



**HAL**  
open science

## A JWST Survey for Planetary Mass Brown Dwarfs in IC 348

K. L. Luhman, C. Alves de Oliveira, I. Baraffe, G. Chabrier, T. R. Geballe, R. J. Parker, Y. J. Pendleton, P. Tremblin

► **To cite this version:**

K. L. Luhman, C. Alves de Oliveira, I. Baraffe, G. Chabrier, T. R. Geballe, et al.. A JWST Survey for Planetary Mass Brown Dwarfs in IC 348. *The Astronomical Journal*, 2024, 167 (1), pp.19. 10.3847/1538-3881/ad00b7 . hal-04684904

**HAL Id: hal-04684904**

**<https://hal.science/hal-04684904v1>**

Submitted on 25 Sep 2024

**HAL** is a multi-disciplinary open access archive for the deposit and dissemination of scientific research documents, whether they are published or not. The documents may come from teaching and research institutions in France or abroad, or from public or private research centers.

L'archive ouverte pluridisciplinaire **HAL**, est destinée au dépôt et à la diffusion de documents scientifiques de niveau recherche, publiés ou non, émanant des établissements d'enseignement et de recherche français ou étrangers, des laboratoires publics ou privés.



Distributed under a Creative Commons Attribution 4.0 International License



# A JWST Survey for Planetary Mass Brown Dwarfs in IC 348\*

K. L. Luhman<sup>1,2</sup> , C. Alves de Oliveira<sup>3</sup> , I. Baraffe<sup>4,5</sup> , G. Chabrier<sup>4,5</sup> , T. R. Geballe<sup>6</sup> , R. J. Parker<sup>7,10</sup> ,  
Y. J. Pendleton<sup>8</sup> , and P. Tremblin<sup>9</sup>

<sup>1</sup> Department of Astronomy and Astrophysics, The Pennsylvania State University, University Park, PA 16802, USA; [kil207@psu.edu](mailto:kil207@psu.edu)

<sup>2</sup> Center for Exoplanets and Habitable Worlds, The Pennsylvania State University, University Park, PA 16802, USA

<sup>3</sup> European Space Agency, European Space Astronomy Centre, Camino Bajo del Castillo s/n, E-28692 Villanueva de la Cañada, Madrid, Spain

<sup>4</sup> Physics & Astronomy Department, University of Exeter, Exeter EX4 4QL, UK

<sup>5</sup> Ecole Normale Supérieure de Lyon, CRAL, CNRS UMR 5574, F-69364, Lyon Cedex 07, France

<sup>6</sup> Gemini Observatory/NSF's NOIRLab, 670 N. Aohoku Place, Hilo, HI 96720, USA

<sup>7</sup> Department of Physics and Astronomy, The University of Sheffield, Hicks Building, Hounsfield Road, Sheffield S3 7RH, UK

<sup>8</sup> Department of Physics, University of Central Florida, Orlando, FL 32816, USA

<sup>9</sup> Université Paris-Saclay, UVSQ, CNRS, CEA, Maison de la Simulation, F-91191, Gif-sur-Yvette, France

Received 2023 July 24; revised 2023 October 3; accepted 2023 October 4; published 2023 December 13

## Abstract

We have obtained images of the center of the star-forming cluster IC 348 with the James Webb Space Telescope and have identified brown dwarf candidates based on their photometry and point-like flux profiles. Low-resolution spectroscopy has been performed on four promising candidates, three of which have molecular absorption bands that indicate late spectral types. Among those late-type objects, the brightest is similar to known young L dwarfs while the other two show the so-called 3.4  $\mu\text{m}$  feature that has been previously observed in the diffuse interstellar medium and in the atmospheres of Saturn and Titan, which has been attributed to an unidentified aliphatic hydrocarbon. Those two objects also exhibit features between 1.1 and 2.6  $\mu\text{m}$  that we identify as the overtone and combination bands for that hydrocarbon. After accounting for the hydrocarbon bands, the remaining spectral features are consistent with youth and inconsistent with field dwarfs. Based on the low extinctions of those objects and the strengths of the overtone and combination bands, we conclude that the hydrocarbon resides in their atmospheres rather than in foreground material. Thus, our detections of the 3.4  $\mu\text{m}$  feature are the first in atmospheres outside of the solar system. The presence of this hydrocarbon is not predicted by any atmospheric models of young brown dwarfs. Based on its luminosity and evolutionary models, the faintest new member of IC 348 has an estimated mass of 3–4  $M_{\text{Jup}}$ , making it a strong contender for the least massive free-floating brown dwarf that has been directly imaged to date.

*Unified Astronomy Thesaurus concepts:* Brown dwarfs (185); L dwarfs (894); Star forming regions (1565); Initial mass function (796); Exoplanet atmospheres (487); T dwarfs (1679); James Webb Space Telescope (2291)

*Supporting material:* data behind figure, machine-readable table

## 1. Introduction

The identification of brown dwarfs at planetary masses ( $\lesssim 15 M_{\text{Jup}}$ ) is important for constraining the minimum mass of the initial mass function and understanding the formation, evolution, and atmospheres of both brown dwarfs and planets. Brown dwarfs have been discovered with masses down to  $\sim 5\text{--}10 M_{\text{Jup}}$  through infrared (IR) imaging surveys of the solar neighborhood (Cushing et al. 2011; Luhman 2014; Kellogg et al. 2015; Schneider et al. 2016; Kirkpatrick et al. 2019; Bardalez Gagliuffi et al. 2020; Meisner et al. 2020) and the nearest young associations (Liu et al. 2013; Gagné et al. 2018; Schneider et al. 2023) and star-forming regions (Alves de Oliveira et al. 2012; Scholz et al. 2012; Esplin et al. 2017; Zapatero Osorio et al. 2017; Lodieu et al. 2018; Esplin & Luhman 2019; Robberto et al. 2020; Bouy et al. 2022). Those surveys have provided few constraints on the existence of

brown dwarfs below 5  $M_{\text{Jup}}$ . Microlensing observations, which have been capable of detecting free-floating Earth-mass planets (Mróz et al. 2017; Kim et al. 2021; Ryu et al. 2021; Gould et al. 2022), are consistent with a mass function that continues to decline into the mass range of  $\sim 1\text{--}5 M_{\text{Jup}}$ , but the minimum mass of brown dwarfs is undetermined (Gould et al. 2022; Chabrier & Lenoble 2023).

Because of their low temperatures, brown dwarfs are brightest at IR wavelengths. The James Webb Space Telescope (JWST; Gardner et al. 2023) offers the greatest sensitivity of any IR telescope to date. Given its modest field of view, JWST is best suited for brown dwarf surveys in compact stellar clusters. The lowest masses can be reached in the nearest compact clusters associated with star-forming regions ( $\sim 300$  pc) since substellar objects are brightest when they are young. Among nearby young clusters, IC 348 in the Perseus molecular cloud (Lada & Lada 1995; Herbig 1998; Herbst 2008) is one of the most appealing targets for JWST because it is relatively rich ( $\sim 500$  known members), is not heavily embedded ( $A_V < 4$ ), and lacks an H II region and the accompanying bright background emission. In addition, IC 348 has been thoroughly searched for stellar and substellar members, resulting in a census that has a high level of completeness down to  $\sim 10 M_{\text{Jup}}$  (Luhman et al. 2016) and extends to lower masses (Alves de Oliveira et al. 2013; Esplin & Luhman 2017; Luhman & Hapich 2020). In this paper, we

\* Based on observations made with the NASA/ESA/CSA James Webb Space Telescope and the Gaia mission.

<sup>10</sup> Royal Society Dorothy Hodgkin Fellow.



Original content from this work may be used under the terms of the [Creative Commons Attribution 4.0 licence](https://creativecommons.org/licenses/by/4.0/). Any further distribution of this work must maintain attribution to the author(s) and the title of the work, journal citation and DOI.

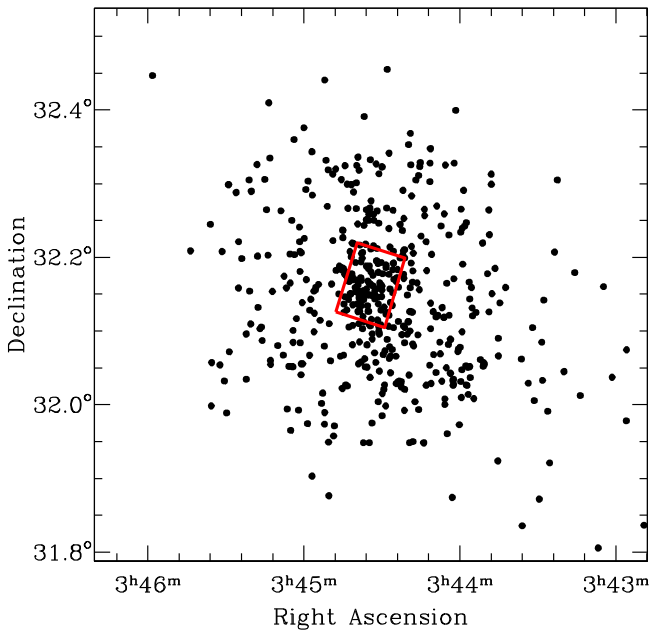


**Figure 1.** Map of the known members of IC 348 and the field imaged by JWST/NIRCam in this study (red box).

present JWST observations in the center of IC 348 that are capable of detecting cluster members with masses down to  $\sim 2 M_{\text{Jup}}$ .

## 2. Imaging

### 2.1. NIRC*am* Observations

We obtained images of a field in the center of IC 348 using NIRC*am* on JWST (Rieke et al. 2005, 2023) through guaranteed time observation (GTO) program 1229 (PI: C. Alves de Oliveira) on 2022 August 28 (UT). NIRC*am* collects simultaneous images through short- and long-wavelength channels (0.7–2.4 and 2.4–5  $\mu\text{m}$ , respectively) for nearly identical areas of sky. The short-/long-wavelength channels contain eight/two 2040  $\times$  2040 detector arrays with pixel sizes of 0 $^{\prime\prime}$ .031/0 $^{\prime\prime}$ .063. For each channel, the detectors cover two 2 $^{\prime}$ .2  $\times$  2 $^{\prime}$ .2 fields that are separated by  $\sim 43^{\prime\prime}$ . For each of those two fields, 5 $^{\prime\prime}$  gaps are present between four detectors in the short-wavelength channel.

The NIRC*am* imaging was performed with the FULLBOX/2TIGHTGAPS dither pattern and a mosaic pattern containing two rows and one column, which covered an area with a size of 6 $^{\prime}$ .0  $\times$  4 $^{\prime}$ .2. In Figure 1, we have plotted a map of the known members of IC 348 (Luhman et al. 2016; Esplin & Luhman 2017; Allers & Liu 2020; Luhman & Hapich 2020)<sup>11</sup> and have marked the boundary of the field observed by NIRC*am*, which encompasses 95 known members. The two rows in the mosaic were observed in separate visits and each covered 3 $^{\prime}$ .0  $\times$  4 $^{\prime}$ .2 with little overlap. At a given position and filter, 1–2 exposures were taken. Each exposure utilized three groups, one integration, and the SHALLOW4 readout pattern,

<sup>11</sup> Lalchand et al. (2022) reported the discovery of three new members of IC 348. Among those objects, we find that WBIS 03435016+3204073 has a classification of young M6 based on our comparison of the spectrum from that study to young standards from Luhman et al. (2017), WBIS 03441864+3218204 has a proper motion from Gaia DR3 that is inconsistent with membership, and WBIS 03451508+3218215 was previously identified as a member by Luhman et al. (2016).

corresponding to an exposure time of 150 s. We selected six filters (three in each of the two channels) in which brown dwarfs should exhibit colors that are distinctive from other astronomical sources, consisting of F140M, F162M, F182M, F277W, F360M, and F444W. The charged time was 2.97 hr.

To compare the bandpasses of these filters to the wavelengths of late-type spectral features, we have plotted the bandpasses in Figure 2 with a spectrum of the L-type companion VHS J125601.92–125723.9b (VHS 1256b; Gauza et al. 2015) obtained with the Near-Infrared Spectrograph (NIRSpec; Jakobsen et al. 2022) on board JWST. The NIRSpec observations of VHS 1256b were planned by Hinkley et al. (2022) and first analyzed by Miles et al. (2023). We show the reduced version of the spectrum produced by Luhman et al. (2023) after binning to a resolution of  $R = 200$ . We have included in Figure 2 the brightest emission feature in the background spectrum extracted from our NIRSpec data in IC 348, which we attribute to polycyclic aromatic hydrocarbons (PAHs). We selected the F360M filter rather than other available NIRC*am* filters at similar wavelengths because it encompasses part of the fundamental band of  $\text{CH}_4$  while avoiding the brightest PAH emission at 3.3  $\mu\text{m}$ .

### 2.2. NIRC*am* Data Reduction

To reduce the NIRC*am* data, we began by retrieving the `uncal` files from the Mikulski Archive for Space Telescopes (MAST) doi:10.17909/6rt2-f215. We processed the data on multiple occasions with the latest available versions of the JWST Science Calibration pipeline and the Calibration Reference Data System (CRDS) context. The NIRC*am* data presented in this study are based on our most recent reduction, which used pipeline version 1.10.2 under context `jwst_1078.pmap`. Detector-level corrections were applied to the `uncal` files using the `calwebb_detector1` pipeline module. The resulting count rate images (`rate`) were processed by the `calwebb_image2` module to produce calibrated unrectified exposures (`cal`). The `calwebb_image3` module registered and combined the exposures for a given filter. Since the two rows in the mosaic pattern were observed in different visits and have few overlapping stars for checking alignment, we applied `calwebb_image3` to the two rows separately, resulting in a pair of adjacent mosaic images for each filter. We used the default values of the parameters for the three pipeline modules with the exception of `steps.tweakreg.skip` in `calwebb_image3`, which was set to `true` for the final reduction. The `tweakreg` routine uses detected sources in individual exposures to refine their world coordinate systems (WCSs) so that the celestial coordinates of stars among overlapping exposures are aligned. However, we were unable to produce satisfactory alignment with `tweakreg`. When that routine was disabled, we found that the point spread functions of stars in the resulting mosaics were as narrow and symmetric as in the individual exposures, indicating that the default WCSs for a given filter and visit did not require refinement.

In addition to creating a mosaic image, `calwebb_image3` identifies sources in that image down to a specified threshold of the signal-to-noise ratio and measures their astrometry and photometry. When inspecting the mosaic images, we found that many well-detected sources in areas with higher background emission were not identified by `calwebb_image3`, which applied primarily to the bands at longer wavelengths. Therefore, we instead used the `starfind` routine in IRAF to

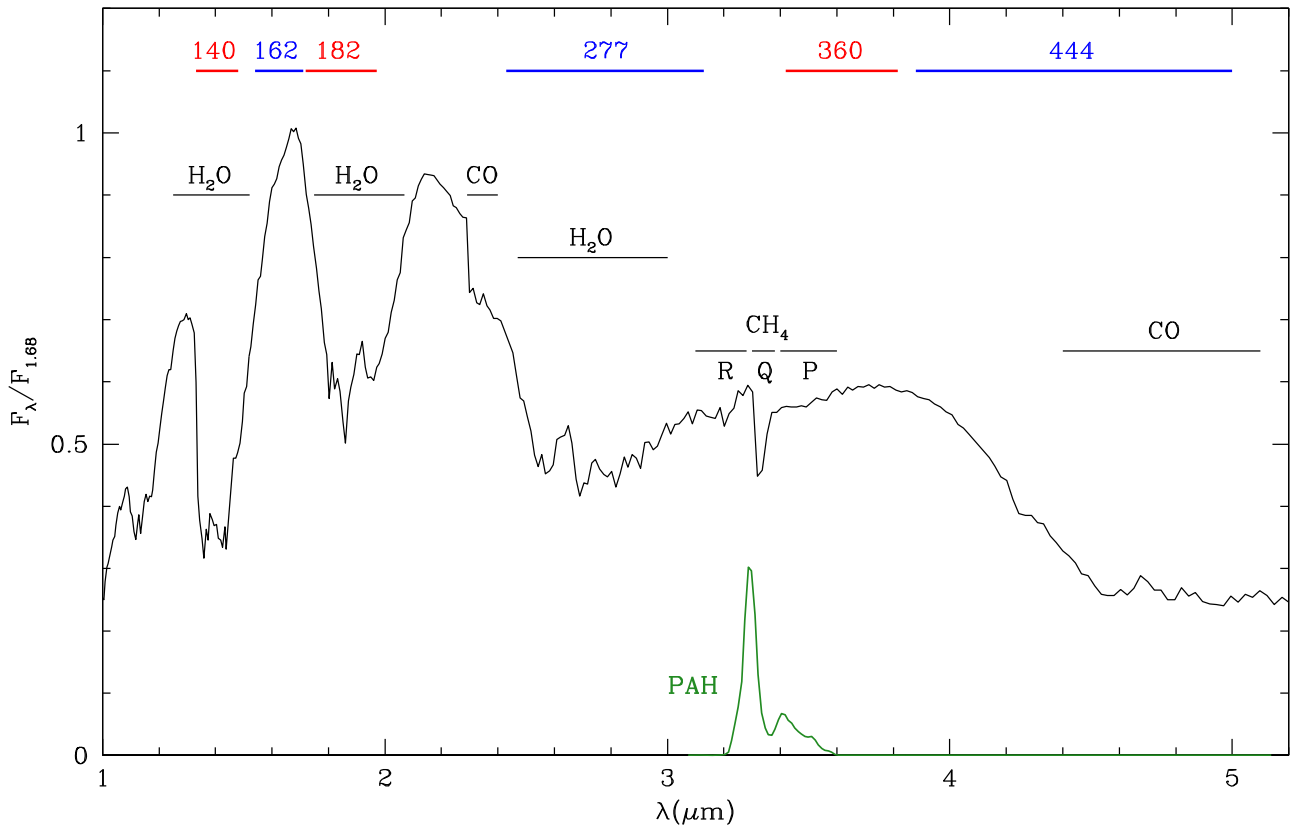


**Figure 2.** JWST/NIRSpec spectrum of the substellar companion VHS 1256b after binning to a resolution of  $R = 200$  (Luhman et al. 2023). We have marked the wavelengths spanned by the six NIRCcam filters selected for imaging of IC 348. We have included a spectrum of background PAH emission extracted from our NIRSpec observations in IC 348.

identify sources in the mosaic images, which appeared to find a larger fraction of the detected sources. For sources that were identified in only a subset of the six filters, we visually inspected the images for detections that had been missed. The pixel coordinates of such detections were measured with `imexamine` in IRAF.

For each of the two rows in the mosaic pattern, we identified matching sources among the catalogs for the six filters and measured the average offsets in R.A. and decl. relative to the catalog for F162M. We applied those offsets to the coordinates in the catalogs to align them to F162M. For each source, we calculated the median of the coordinates from the filters with detections. We applied offsets to those median coordinates to align them to the reference frame of the Gaia mission (Perryman et al. 2001; de Bruijne 2012; Gaia Collaboration et al. 2016) using detections (including those that were saturated) of sources from the third data release of Gaia (DR3; Gaia Collaboration et al. 2021, 2023). We sought to reject spurious detections by retaining only the sources that were identified in multiple filters. For the multiband sources, we inspected the images to remove remaining spurious detections, most of which occurred near saturated stars.

Each of the two final band-merged catalogs (for the two rows in the mosaic) contained  $\sim 300$  sources. Five of the 95 known members of IC 348 encompassed by the NIRCcam images have unsaturated detections in any of the filters. We measured three sets of aperture photometry for the sources using `phot` in IRAF for apertures with radii of 2, 3, and 4 pixels. The inner and outer radii of the sky annuli were 4 and 8 pixels, respectively. The resulting photometry was calibrated using the

Vega aperture photometry produced by the `calwebb_image3` pipeline module for sources appearing in our catalogs. We use the 3 pixel photometry for most purposes in this study unless indicated otherwise.

### 2.3. Identification of Brown Dwarf Candidates

Faint galaxies are one source of contamination in our survey for brown dwarfs. Given its high angular resolution, NIRCcam is capable of resolving many of those galaxies. To distinguish between point sources and resolved galaxies, we use the median of the differences of the 2 and 4 pixel aperture photometry from among the bands in which a given source is detected. In Figure 3, we have plotted  $m_{162}$  versus that median difference for all sources in the two catalogs produced in Section 2.2. The median differences exhibit two distinct populations where those above and below  $\sim 0.1$  correspond to extended and point sources, respectively.

The faintest known members of IC 348 have spectral types of early L (Alves de Oliveira et al. 2013; Luhman et al. 2016; Esplin & Luhman 2017; Luhman & Hapich 2020), so new members at fainter magnitudes are expected to have spectral types of L and T. After examining various color-color diagrams that are available for our NIRCcam data, we found that  $m_{162} - m_{444}$  versus  $m_{360} - m_{444}$  provides the best discrimination between brown dwarfs at those types and other sources. We show that diagram in Figure 4, where we also include a diagram of  $m_{162}$  versus  $m_{360} - m_{444}$ . In both diagrams, the symbols indicate whether the sources are point-like or extended based on the metric in Figure 3, where we have adopted a threshold of 0.1 between the two classifications. We have

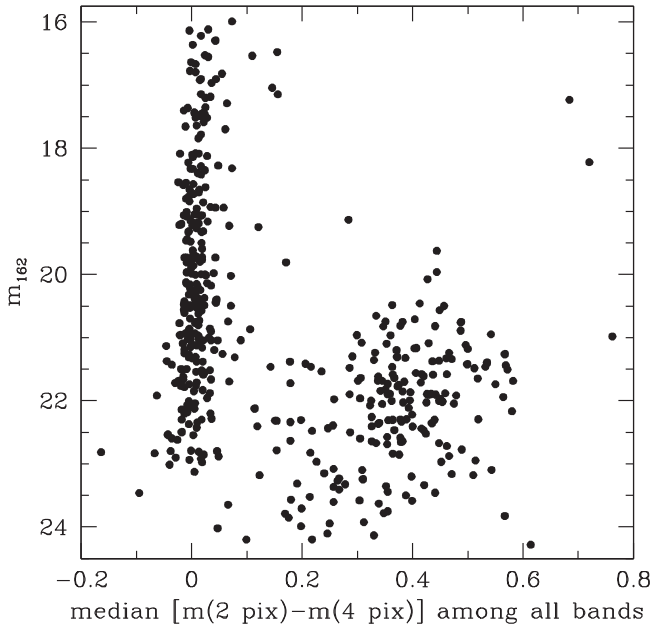


**Figure 3.**  $m_{162}$  vs. the median difference between 2 and 4 pixel aperture photometry among the available bands for sources in NIRCcam images of IC 348. This metric is used to classify the sources as point-like ( $<0.1$ ) or extended ( $\geq 0.1$ ).

marked the two known members that appear in the NIRCcam images and are not saturated in the plotted bands, which have spectral types of early L. In the color-color diagram, we also show the colors of the young L-type companion TWA 27B (2M 1207B; Chauvin et al. 2004) from Luhman et al. (2023), which is a member of the TW Hya association (10 Myr; Luhman 2023).

In Figure 4, TWA 27B and the known brown dwarfs in IC 348 are redder than most point sources in  $m_{360} - m_{444}$ . We expect that cluster members at fainter magnitudes and later spectral types will be progressively redder in that color (Kirkpatrick et al. 2011). In a color like  $m_{162} - m_{444}$ , young objects become redder from early to late L types and may reverse to bluer colors beyond the L/T transition (Filippazzo et al. 2015; Liu et al. 2016), so new L/T-type members of IC 348 could be either redder or bluer than TWA 27B and the known L-type cluster members in  $m_{162} - m_{444}$ . The fact that TWA 27B is one of the reddest known young L dwarfs (Luhman et al. 2023) suggests that new members are probably not significantly redder than it in  $m_{162} - m_{444}$  unless they have excess emission in  $m_{444}$  from circumstellar disks.

The color-magnitude diagram in Figure 4 contains many sources that are faint and red, but most of them are extended based on the metric in Figure 3 and are likely to be galaxies. Most of those probable galaxies are redder in  $m_{162} - m_{444}$  than TWA 27B and the known brown dwarfs in IC 348, as shown in the color-color diagram in Figure 4. Among the point sources in Figure 4, several are redder than the known members in  $m_{360} - m_{444}$ , and thus are considered to be brown dwarf candidates. The candidates that were observed with spectroscopy are circled and are labeled with the source numbers that we have assigned to them (Section 3). A point source can be mistakenly classified as extended if it is close to another object, so we inspected the NIRCcam images of sources that satisfied the criterion for extended emission and that have colors in Figure 4 that are consistent with an L/T-type member. We

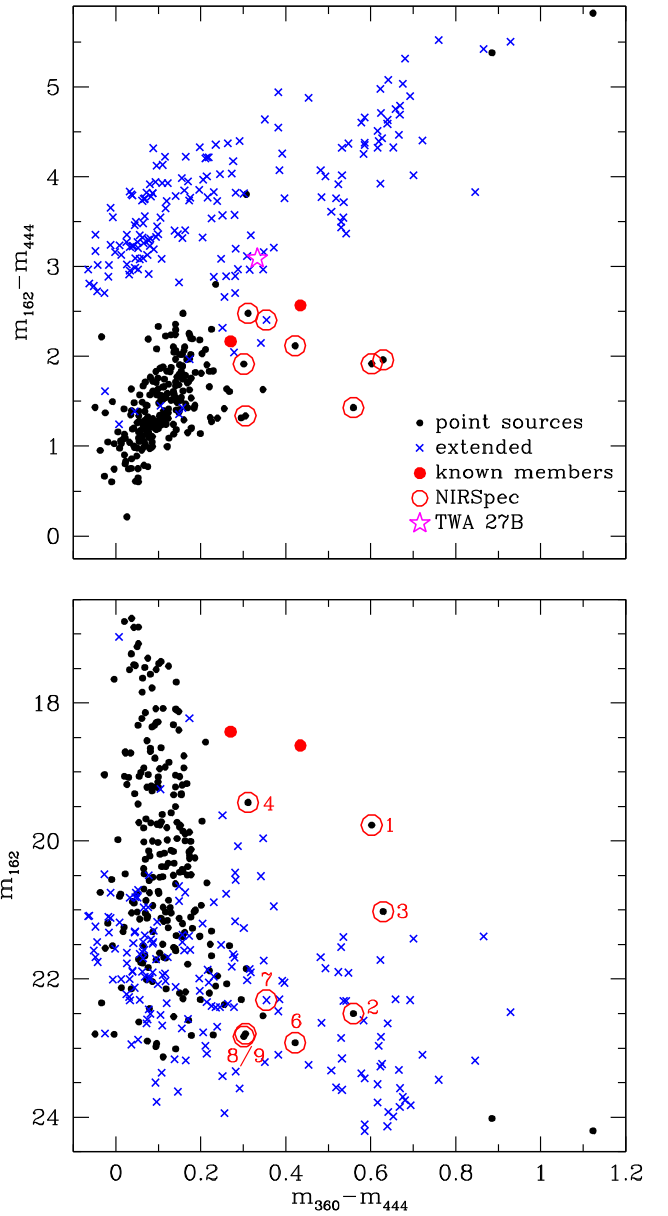


**Figure 4.**  $m_{162} - m_{444}$  and  $m_{162}$  vs.  $m_{360} - m_{444}$  for sources in NIRCcam images of IC 348. The symbols indicate whether the sources are point-like (filled circles) or extended (crosses) based on the metric from Figure 3. We have marked the known members of IC 348 that are within the NIRCcam images and are not saturated (red filled circles). We have performed NIRSpec observations on eight candidates for new members (open circles), which are labeled with the source numbers from Table 1. Colors for the planetary mass companion TWA 27B are included in the top diagram (open star, Luhman et al. 2023).

identified one point source of this kind, which was retained as a brown dwarf candidate and observed with spectroscopy (source 7). In addition to identifying brown dwarf candidates in the diagrams that use  $m_{162}$ ,  $m_{360}$ , and  $m_{444}$ , we also checked for sources that are red in  $m_{360} - m_{444}$  and are too red in  $m_{162} - m_{444}$  to be detected in  $m_{162}$ , but no point sources of that kind are in our catalogs.

We briefly discuss the point sources from Figure 4 that are red in  $m_{360} - m_{444}$  but were not observed spectroscopically. The reddest two point sources in  $m_{360} - m_{444}$  and  $m_{162} - m_{444}$  seem too red in the latter color to be brown dwarfs ( $>2$  mag redder than TWA 27B). Two other point sources have colors in

Figure 4 that more closely resemble those of known brown dwarfs. Both of those objects are similar to TWA 27B in  $m_{360} - m_{444}$  while in  $m_{162} - m_{444}$  one is 0.7 mag redder and the other is 1.5 mag bluer. None of these four objects are as blue as TWA 27B and the known IC 348 members in  $m_{162} - m_{182}$  (Figure 2), so we do not consider them to be strong candidates for substellar members of IC 348.

One of the candidates selected for spectroscopy in Section 3, source 1, has been previously detected in deep optical images obtained with the Wide Field Planetary Camera 2 (WFPC2) on the Hubble Space Telescope (Luhman et al. 2005). Because of the high angular resolutions of the WFPC2 and NIRCcam images and the long baseline that they span (21 years), these data provide useful constraints on the proper motion of the candidate. Between the WFPC2 and NIRCcam images, source 1 is motionless relative to background stars at a level ( $\lesssim 6$  mas  $\text{yr}^{-1}$ ) that is consistent with membership in the cluster (Luhman et al. 2016).

### 3. Spectroscopy

#### 3.1. NIRS<sub>pec</sub> Observations

We observed brown dwarf candidates identified in Section 2.3 using the multi-object spectroscopy (MOS) mode of NIRS<sub>pec</sub> on JWST (Ferruit et al. 2022) through GTO program 1229 (PI: C. Alves de Oliveira). The MOS mode utilizes the microshutter assembly (MSA), which consists of four quadrants that each contain  $365 \times 171$  shutters. The quadrants are separated by  $23''$  in the dispersion direction and  $37''$  in the spatial direction. Individual shutters have angular sizes of  $0''.2 \times 0''.46$ . Adjacent shutters are separated by bars that have widths of  $\sim 0''.07$ . The size of the field spanned by the MSA is  $3''.6 \times 3''.4$ . The NIRS<sub>pec</sub> focal plane contains two  $2048 \times 2048$  detector arrays with pixel sizes of  $0''.103 \times 0''.105$ .

The PRISM disperser was selected for our observations because it offers the best sensitivity and the widest wavelength coverage (0.6–5.3  $\mu\text{m}$ ) among the available options. The spectral resolution of the PRISM data ranges from  $\sim 40$  to 300 from shorter to longer wavelengths. Low resolution is adequate for measuring the broad molecular bands that appear in spectra of brown dwarfs, as illustrated in Figure 2.

We designed MSA configurations for the brown dwarf candidates using the MSA Planning Tool (MPT) in the Astronomer’s Proposal Tool. When running MPT, we adopted the aperture position angle assigned to our program. We configured MPT so that each target is observed in three adjacent shutters that are equivalent to a single  $0''.2 \times 1''.5$  slitlet. To be considered for spectroscopy at a given pointing, MPT requires that a target’s position in a shutter is no closer than a specified distance from the shutter’s edge. A larger value for that minimum distance ensures less slit loss at the possible expense of fewer observable targets. Five options are available, ranging from  $0''$  to  $0''.091$ . We selected the second largest value, which is  $0''.072$ .

The input catalog of targets for MPT can include weights (priorities) that are used in identifying an optimal MSA configuration. We assigned the highest weights to four promising targets from Section 2.3, which have source numbers of 1 through 4 (Figure 4). Lower weights were given to five less promising candidates (sources 5–9) and five known members of IC 348 (sources 10–14). For those known

members, we selected objects that (1) are close enough to the candidates that they might be observable in the same MSA configuration, (2) have spectral types of late-M or L, and (3) are faint enough that they would not saturate in the NIRS<sub>pec</sub> data. For known members that are located outside of the NIRCcam images, we used ground-based astrometry (Luhman et al. 2016) aligned to the reference frame of the NIRCcam catalogs.

Within a selected range of pointings, MPT identifies the pointing that maximizes the total weight of the observable targets. The output for an optimal configuration includes the wavelength range that falls on the detector arrays for each target. We divided the area surrounding the candidates into a grid of small subfields and used MPT to identify the optimal MSA configuration for each subfield. The four high-priority candidates can fit within a single MSA field of view. In addition, they appear in the same row (half) of the NIRCcam mosaic, so they should have precise relative astrometry that would allow them to be reliably observed in the same MSA configuration. However, MPT did not identify a single configuration that would observe all four of those candidates. Therefore, from among the optimal configurations in the various subfields, we searched for a pair of configurations that were optimal in terms of the following considerations: (1) the four high-priority candidates appear in at least one configuration; (2) the fainter high-priority candidates appear in both configurations; (3) the number of low-priority candidates and known members; (4) wide wavelength coverages, particularly for the high-priority candidates; (5) availability of the recommended number (eight) of suitable stars for target acquisition; and (6) a pair of configurations separated by less than the visit splitting distance ( $65''$ ) so that they could be observed in single visit. In the two MSA configurations that we adopted, the first included sources 1, 2, 3, 8, and 9 and the second included sources 2, 3, 4, 6, 7, and 13. Thus, the pair of configurations provided data for the four high-priority candidates (the faintest two candidates observed in both configurations), four low-priority candidates, and one known member. For one of the two configurations, the data for source 3 did not extend below 1.2  $\mu\text{m}$ . The spectrum for the known member (source 13/LRL 30057) was truncated below 2.9  $\mu\text{m}$ . All other observations had full coverage of 0.6–5.3  $\mu\text{m}$ .

The NIRS<sub>pec</sub> targets are listed in Table 1, which contains source numbers, coordinate-based names, equatorial coordinates, spectral classifications, a flag for spectroscopic evidence of youth, luminosity estimates, and NIRCcam photometry.

The observations with the two MSA configurations were performed on 2023 February 3 (UT). At each of the three nod positions, one exposure was taken, which utilized 92 groups, one integration, and the NRSIRS2RAPID readout pattern. In a given MSA configuration, the total exposure time for three exposures was 4070 s. The charged time was 4.55 hr.

#### 3.2. NIRS<sub>pec</sub> Data Reduction

The reduction of the NIRS<sub>pec</sub> data began with the retrieval of the uncal files from MAST doi: [10.17909/6rt2-f215](https://doi.org/10.17909/6rt2-f215). Within the JWST Science Calibration pipeline (version 1.9.4 with CRDS context `jwst_1041.pmap`), we applied the `calwebb_detector1` module to the uncal files, which produced count rate images (`rate`). Several steps were performed on the `rate` images with the `calwebb_spec2` module, including flat fielding and background subtraction. The resulting `cal` images were processed with the `calwebb_spec3` module,

**Table 1**  
Sources in IC 348 Observed with NIRSPEC

Column Label	Description
ID	Source number
Name	IC 348 IRS
RAdeg	R.A. (ICRS) <sup>a</sup>
DEdeg	decl. (ICRS) <sup>a</sup>
SpType	Spectral type <sup>a</sup>
young	Young?
Lbol	Log $L/L_{\odot}$
e_Lbol	Error in Lbol
m140mag	F140M NIRCam magnitude
e_m140mag	Error in m140mag
m162mag	F162M NIRCam magnitude
e_m162mag	Error in m162mag
m182mag	F182M NIRCam magnitude
e_m182mag	Error in m182mag
m277mag	F277W NIRCam magnitude
e_m277mag	Error in m277mag
m360mag	F360M NIRCam magnitude
e_m360mag	Error in m360mag
m444mag	F444W NIRCam magnitude
e_m444mag	Error in m444mag

**Note.**

<sup>a</sup> The coordinates and spectral type are from Luhman et al. (2016) for source 13. For all other sources, they are from NIRCam and NIRSPEC data in this work.

(This table is available in its entirety in machine-readable form.)

which registered and combined the noded 2D exposures for each target and extracted its spectrum. We selected a width of 5 pixels ( $0''.53$ ) for the extraction apertures. For each target, we measured its position along the slit in the combined 2D exposures, which was used as the center of the extraction aperture. For a target observed in both MSA configurations, the two extracted spectra were combined.

We performed a separate reduction using a custom pipeline derived from the pipeline developed by the ESA NIRSPEC Science Operations Team (Ferruit et al. 2022) and based on the workflow and algorithms described in Alves de Oliveira et al. (2018). Additional details regarding the custom pipeline will be presented in a future NIRSPEC GTO collaboration paper (S. Carniani et al. 2023, in preparation). We briefly describe the main data reduction steps. In the first stage, the master bias frame and dark current were subtracted and artifacts such as “snowballs” (Böker et al. 2023) were corrected. For each exposure, the count rate per pixel was estimated by fitting the slope of individual ramps while identifying and removing jumps due to cosmic rays and flagging saturated pixels. We then performed a pixel-by-pixel background subtraction using the average of the exposures at the other two nods. The individual 2D spectra from each shutter were flat fielded and corrected for illumination by the spectrograph optics and the wavelength-dependent throughput of the dispersing element. The wavelength and flux calibrations were applied. For each of the resulting 2D images, we measured the position of the target along the slit and extracted its spectrum. The extracted spectra from the individual nods were then combined.

The reduced spectra from the NIRSPEC GTO pipeline were similar to or better than those from the JWST Science Calibration Pipeline in terms of spectral resolution and

signal-to-noise ratios. Therefore, we have adopted the reductions from the NIRSPEC GTO pipeline.

When designing the MSA configurations, MPT predicted that source 3 would be well centered in the shutters of its slitlet in the first configuration and would be closer to a shutter corner in the second one. As a result, the second observation of source 3 was expected to experience increasing slit loss at longer wavelengths, and that is indeed reflected in the slopes of the reduced spectra. To correct for that effect, we have multiplied the second set of spectra for source 3 by a low-order polynomial so that they have the same spectral slope as the spectra from the first configuration.

In the NIRCam images, source 7 is projected against a resolved galaxy. Background subtraction for a given nod can be performed with one or both of the other two nods. For each nod, we determined whether using one or both of the other nods would minimize the galaxy emission that was subtracted at the position of source 7. In the end, we used the second nod as the background for both the first and third nods. We did not use the spectrum of source 7 from the second nod since the other nods did not provide adequate background subtraction. For reference, the first, second, and third nods respectively correspond to the middle, top, and bottom shutters of a slitlet in the coordinate system of the detector arrays.

The spectral images of source 8 show extended emission along the slit, primarily at shorter wavelengths. The origin of that emission is not evident from the NIRCam images, where source 8 appears as an isolated point source. The extended emission in the NIRSPEC data may be below the detection limits of the NIRCam images. As with source 7, we experimented with the available combinations of nods for the background subtraction to minimize the extended emission that was subtracted from source 8. We made use of only the second nod, for which the third nod provided a measurement of the background.

For the eight NIRSPEC targets that are located within the NIRCam images, we have used the photometry from those data to flux calibrate the reduced NIRSPEC spectra. The one remaining target, source 13, is outside of the NIRCam images and lacks accurate photometry within the wavelength range of its NIRSPEC data ( $2.9\text{--}5.3\ \mu\text{m}$ ), so we have adopted the flux calibration produced by the NIRSPEC GTO pipeline.

The reduced NIRSPEC data are presented in Figure 5. As in Figure 2, we have included a spectrum of the brightest PAH feature appearing in the background emission in the NIRSPEC data. Based on the 2D spectral images, the bright emission line in the spectrum of source 7 arises from the galaxy that surrounds it. The spectra of two of the fainter sources, 2 and 7, contain negative and positive residuals, respectively, that correspond to the brightest PAH emission and reflect imperfect background subtraction.

## 4. Spectral Classification

### 4.1. Sources 2, 4, and 6–9

We wish to use the NIRSPEC data to determine whether each brown dwarf candidate is cool and young, and hence a likely substellar member of IC 348. The spectra of sources 2, 6, 7, and 9 contain  $\text{H}_2\text{O}$  absorption bands (see Figure 5) that are too weak for young brown dwarfs (Luhman et al. 2017) and are consistent with mid-M field dwarfs (Rayner et al. 2009). We classify these objects as reddened background field dwarfs. Source 8 lacks clear detections of spectral features. The

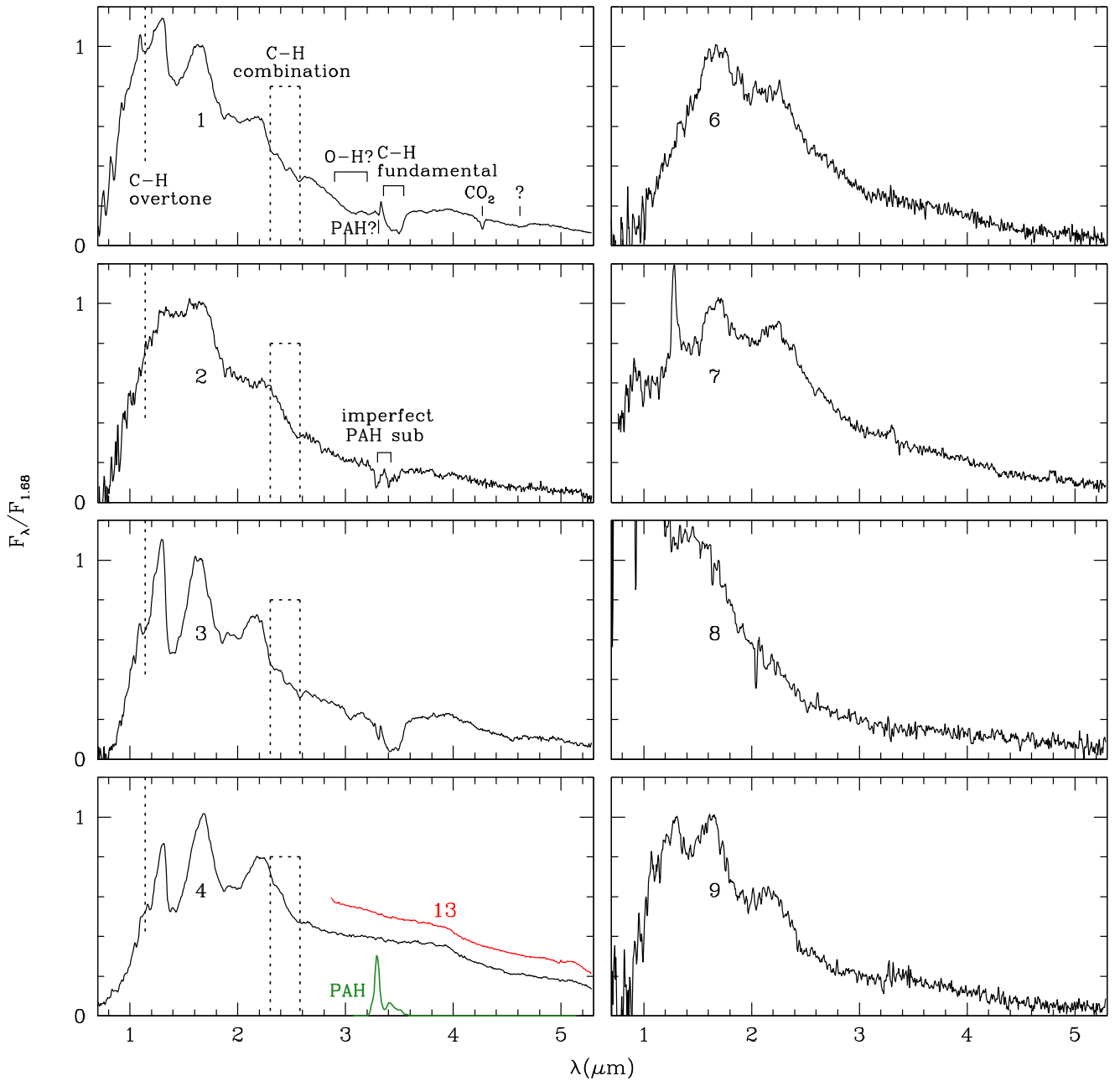


**Figure 5.** JWST/NIRSpec spectra of brown dwarf candidates selected from NIRCcam images of IC 348 (Figure 4). The spectra are labeled with the source numbers from Table 1. We also show NIRSpec data for a known cluster member (source 13), which has been normalized to source 4 at  $3.9 \mu\text{m}$  and shifted upward. The dotted lines mark absorption features in sources 1 and 3 that we attribute to overtone and combination bands of C–H stretching modes in the same carrier that produces the fundamental band at  $3.4 \mu\text{m}$ . Those wavelengths are also marked in the spectra of sources 2 and 4 for reference. We have included a spectrum of the brightest PAH feature appearing in the background emission in the NIRSpec data.

(The data used to create this figure are available.)

absence of strong  $\text{H}_2\text{O}$  absorption indicates that it is a background star or a galaxy. It is not surprising that sources 6–9 are nonmembers given their photometry (Figure 4), as discussed in Section 2.3.

Among the three remaining candidates, source 4 has strong  $\text{H}_2\text{O}$  bands near  $1.4$  and  $1.9 \mu\text{m}$  and a triangular  $H$ -band continuum that is indicative of youth (Lucas et al. 2001). If reddening is allowed as a free parameter, its spectrum at  $<2.5 \mu\text{m}$  agrees well with data for young L dwarfs in the field (Cruz et al. 2009, 2018) and in IC 348 (Alves de Oliveira et al. 2013; Luhman et al. 2016; Esplin & Luhman 2017;

Luhman & Hapich 2020) and the young L0–L5 standards from Luhman et al. (2017). At  $>2.5 \mu\text{m}$ , source 4 closely resembles the known member that was observed by NIRSpec, source 13 (Figure 5), which has a spectral type of M9–L3 (Luhman et al. 2016). Therefore, we classify source 4 as an L-type member of IC 348.

#### 4.2. Anomalous Features in Sources 1 and 3

The spectra of sources 1 and 3 have strong  $\text{H}_2\text{O}$  bands that indicate late spectral types, but they also show anomalous



features that are not immediately attributable to either young brown dwarfs or field dwarfs. We consider the possibilities that these objects are cluster members or field dwarfs in the foreground or background of the cluster and that the anomalous features arise from their atmospheres, the interstellar medium (ISM) in the foreground or background of IC 348, the molecular cloud that surrounds the cluster, or edge-on circumstellar disks. Late-type giants can have H<sub>2</sub>O absorption bands, but sources 1 and 3 are too faint to be giants in the Galaxy. For instance, M giants in the Galaxy’s disk have  $M_H \sim -3$  to  $-6$  (Li et al. 2023), which would correspond to distances of  $\gtrsim 300$  kpc for the apparent magnitudes of sources 1 and 3.

Several features are detected in the spectra of sources 1 and 3 that are absent from the data for source 4. Both candidates exhibit a strong absorption band near 3.4–3.5  $\mu\text{m}$ , which aligns closely with the so-called 3.4  $\mu\text{m}$  feature that has been observed in highly reddened sight lines through the diffuse ISM in the Milky Way, particularly toward the Galactic center (Soifer et al. 1976; Willner et al. 1979; Butchart et al. 1986; Chiar et al. 2013), and in other galaxies (Wright et al. 1996; Geballe et al. 2006; Dartois et al. 2007), a protoplanetary nebula (Lequeux & Jourdain de Muizon 1990; Chiar et al. 1998), carbonaceous meteorites (Wdowiak et al. 1988; Ehrenfreund et al. 1991; de Vries et al. 1993; Pendleton & Allamandola 2002), interplanetary and cometary dust (Matrajt et al. 2005; Keller et al. 2006; Sandford et al. 2006), and the atmospheres of Saturn and Titan (Bellucci et al. 2009; Kim et al. 2012; Robinson et al. 2014; Dalba et al. 2015; Maltagliati et al. 2015). This feature has been attributed to fundamental stretching modes of C–H bonds in aliphatic hydrocarbons that contain groups of CH<sub>2</sub> and CH<sub>3</sub> (Sandford et al. 1991; Pendleton et al. 1994; Pendleton & Allamandola 2002). The profiles of the 3.4  $\mu\text{m}$  feature in sources 1 and 3 differ from those observed in the diffuse ISM (e.g., Geballe et al. 2021), suggesting different relative abundances of the CH<sub>2</sub> and CH<sub>3</sub> groups. For reference, the 3.4  $\mu\text{m}$  feature roughly coincides with the P branch in the CH<sub>4</sub> fundamental band, as illustrated in Figure 2.

In the spectra of sources 1 and 3, additional absorption features occur near 1.14, 2.3–2.6, 3, and 3.3  $\mu\text{m}$ , as indicated in Figure 5. Source 1 also has a feature at 4.27  $\mu\text{m}$  and broad shallow absorption near 4.6  $\mu\text{m}$ . In Section 4.4, we deduce that the 1.14 and 2.3–2.6  $\mu\text{m}$  absorption arises from the overtone and combination bands of the C–H stretching modes that produce the 3.4  $\mu\text{m}$  feature. The 3  $\mu\text{m}$  feature could arise from O–H stretching in H<sub>2</sub>O ice or an alcohol (e.g., ethanol or methanol) or C–H stretching in an alkyne. The 4.27  $\mu\text{m}$  line is probably CO<sub>2</sub> and the 4.6  $\mu\text{m}$  absorption may originate from CO, OCN<sup>−</sup> (Lacy et al. 1984; Pendleton et al. 1999; McClure et al. 2023), or C≡C stretching in an alkyne. For the CO<sub>2</sub> feature, it is difficult to distinguish between gas and ice at the low resolution of our data (Aikawa et al. 2012). Next to the 3.4  $\mu\text{m}$  band in source 3, a separate weaker feature appears at 3.303  $\mu\text{m}$ . The same feature may be present in the spectrum of source 1, but if so, it is blended with the broad trough of absorption near 3  $\mu\text{m}$ . One possible carrier for that 3.3  $\mu\text{m}$  feature are PAHs. In theory, the 3.3  $\mu\text{m}$  line could arise from oversubtraction of the background PAH emission, but we find no evidence for that in the 2D background-subtracted images (no negative residuals at 3.3  $\mu\text{m}$  along the slit). In addition, the line strength is similar among the individual nods (three for

source 1 and six for source 3), which is unlikely to be true if the line arises from imperfect background subtraction.

#### 4.3. Comparison of Sources 1 and 3 to Standards

We have compared the NIRSpect data for sources 1 and 3 to dwarf and young standards across a range of spectral types and reddenings. In the top two rows of Figure 6, we compare source 1 to a young standard (M5.5; Luhman et al. 2017) and a field dwarf (M7V; vB 8; Cushing et al. 2005) that match the 1.4  $\mu\text{m}$  H<sub>2</sub>O band and we compare source 3 to typical field dwarfs at L5 and L8, which span the range of types that match the 1.4  $\mu\text{m}$  H<sub>2</sub>O band. The L5 spectrum is a composite of GJ 1001B at  $<2.5$   $\mu\text{m}$  (Burgasser 2007) and GJ 1001B, 2MASS J05395200−0059019, and 2MASS J22244381−0158521 at  $>2.5$   $\mu\text{m}$  (Sorahana & Yamamura 2012). The L8 spectrum is a composite of the L8 field standard from Cruz et al. (2018) at  $<2.5$   $\mu\text{m}$  and 2MASS J15232263+3014562 and SDSS J083008.12+482847.4 at  $>2.5$   $\mu\text{m}$  (Sorahana & Yamamura 2012). The comparison spectra have been binned to the resolution of the NIRSpect data and reddened to match the 1.3–1.7  $\mu\text{m}$  slopes of sources 1 and 3.

In Figure 6, source 1 differs from both the young M5.5 standard and the M7V field dwarf in terms of the 1.14  $\mu\text{m}$  feature, the shape of the *H*-band peak, and the shape of the *K*-band continuum. Source 1 is also bluer at 0.8–1.1  $\mu\text{m}$  than the reddened field dwarf. Since the discrepancies in the *K* band are highly wavelength dependent, excess emission from a disk cannot explain them. Source 1 is much too faint to be a cluster member with a spectral type of M5.5–M7 unless it is seen primarily in scattered light because of an edge-on disk. The latter might seem like a possible source of the  $>2.5$   $\mu\text{m}$  features, but edge-on disks normally exhibit much stronger absorption at 3  $\mu\text{m}$  (from H<sub>2</sub>O ice) and none have been found to show the 3.4  $\mu\text{m}$  band, at least prior to JWST (Aikawa et al. 2012; Terada et al. 2012). The comparison of source 1 to the M7 dwarf in Figure 6 suggests that the former is redder at longer wavelengths. Based on the NIRSpect data, we find that source 1 is  $\sim 0.8$  mag redder in  $K_s - W2$  than typical M7 dwarfs (Kirkpatrick et al. 2011), which is much larger than the level of reddening that was required for matching the near-infrared (NIR) spectral slope.

As mentioned earlier, the L5 and L8 spectra that are shown in Figure 6 with source 3 span the spectral types of field dwarfs that match the depth of the 1.4  $\mu\text{m}$  H<sub>2</sub>O band. L5 does not reproduce the 1.14  $\mu\text{m}$  absorption or the shape of the *H*-band peak. L8 better matches those features but differs in the strength of the band at 1.8–2  $\mu\text{m}$ . Both field dwarfs have much stronger absorption at 2.5–3  $\mu\text{m}$  (H<sub>2</sub>O) and  $>4.4$   $\mu\text{m}$  (CO) than source 3. Those bands are weak in young L dwarfs, as illustrated in source 4 (Figures 5 and 6) and TWA 27B (Luhman et al. 2023), indicating that source 3 is young as well.

#### 4.4. Comparison of Sources 1, 3, and 4

In the bottom two rows of Figure 6, sources 1 and 3 are compared to each other and to source 4. Sources 1 and 3 differ in their 0.8–1.2  $\mu\text{m}$  slopes and the depths of their absorption at 1.4  $\mu\text{m}$ , but they have similar *H*-band peaks and they share the features at 1.14, 2.3–2.6, and 3.4  $\mu\text{m}$ . In particular, Figure 6 illustrates the close agreement in the structure of the absorption at 2.3–2.6  $\mu\text{m}$  between the two objects. Meanwhile, they lack

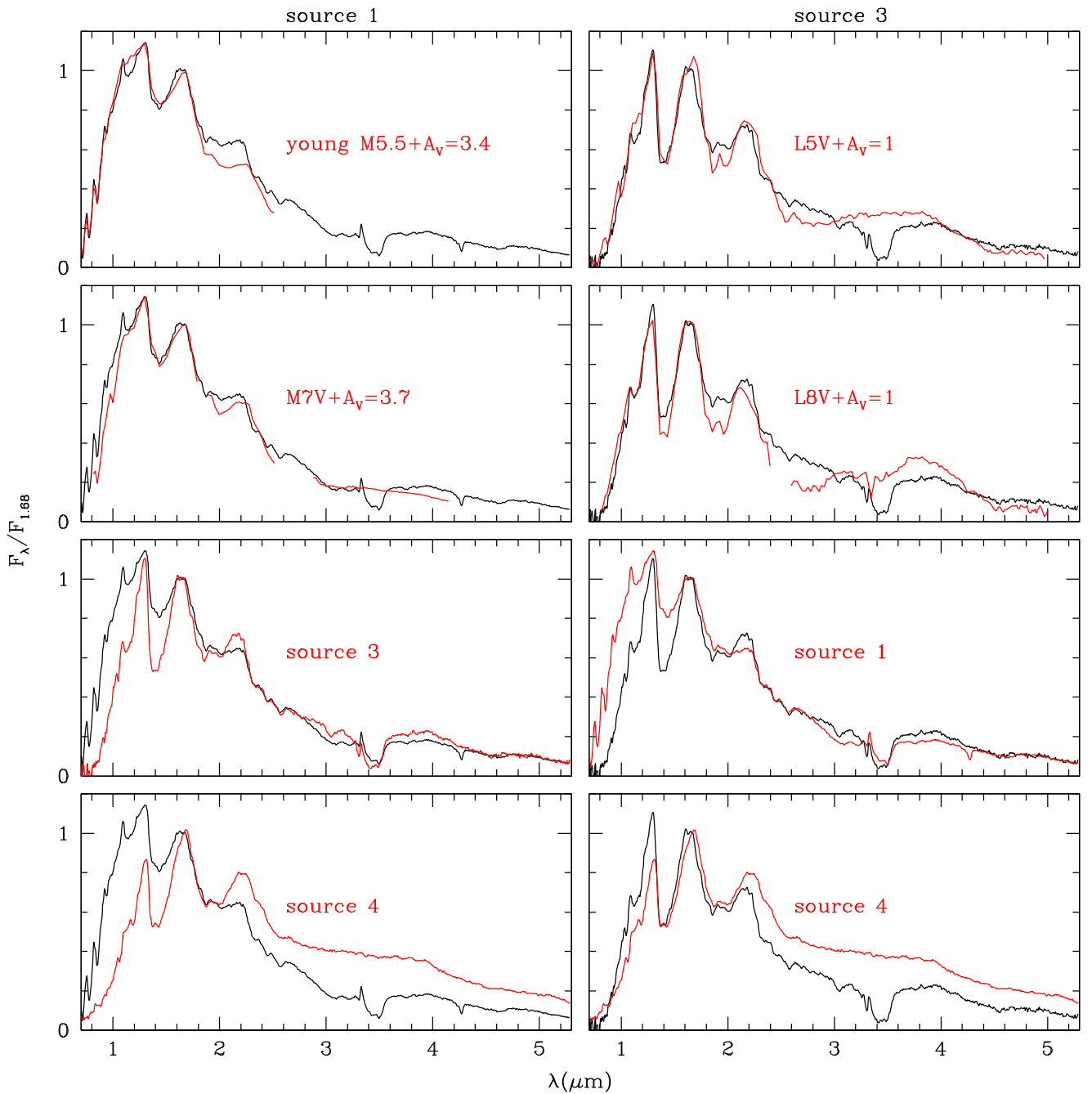


**Figure 6.** JWST/NIRSpec spectra of sources 1 and 3 (left and right, black) compared to various other spectra (red).

the triangular shape for the  $H$ -band peak that is present in source 4 and other previously observed young L dwarfs.

To better isolate the features in sources 1 and 3 that are anomalous relative to normal young objects, we have divided source 1 by the reddened young M5.5 standard from Figure 6 and we have divided source 3 by source 4. The spectrum of the M5.5 standard does not cover the full wavelength range of the NIRSpec data, but it is sufficient for examining the anomalous features at  $<2.5 \mu\text{m}$  in source 1. To facilitate the comparison of features in the divided spectra, we have divided each spectrum by a low-order polynomial fit to the continuum. The resulting spectra are shown in Figure 7. Both spectra contain the previously noted features at 1.14 and 2.3–2.6  $\mu\text{m}$  as well as features near 1.4 and 1.7  $\mu\text{m}$  that were not obvious in the

spectra of sources 1 and 3 because of overlap with  $\text{H}_2\text{O}$  bands. In theory, the absorption at 1.4  $\mu\text{m}$  in the divided spectra could reflect mismatches in the strengths of the  $\text{H}_2\text{O}$  bands. However, that feature and all of the others discussed here closely coincide with the overtone, combination, and fundamental bands for C–H stretching in a variety of hydrocarbons (Clark et al. 2009; Izawa et al. 2014), as illustrated in Figure 7, where we have included a reflectance spectrum of pentane ( $\text{C}_5\text{H}_{12}$ ; Clark et al. 2009). Thus, the anomalous NIR features in sources 1 and 3 are the overtone and combination bands that accompany the fundamental band at 3.4  $\mu\text{m}$ , and most of the departures of these objects from the spectra of known young M/L-type objects (i.e., shape of the  $H$ -band peak) are explained by an unidentified hydrocarbon, whether it is in their atmospheres or

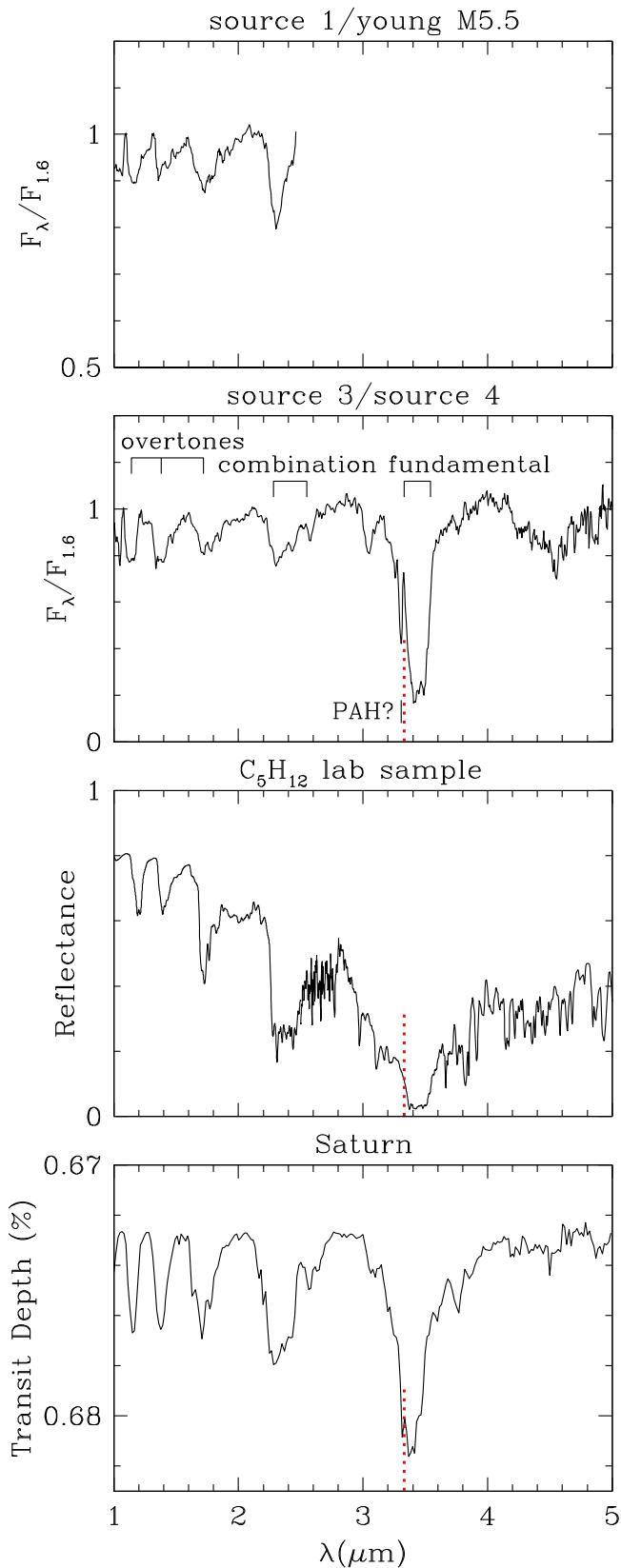


**Figure 7.** Spectra of sources 1 and 3 divided by the spectra of normal young objects (M5.5 standard and source 4), a laboratory reflectance spectrum of  $C_5H_{12}$  (Clark et al. 2009), and a transmission spectrum of Saturn (Dalba et al. 2015). The strongest features in all spectra correspond to fundamental, overtone, and combination bands of C–H stretching modes. For reference, the central wavelength of the Q branch of  $CH_4$  is marked by the red dotted line (see Figure 2).

in the ISM. Meanwhile, even after accounting for the features of that hydrocarbon, source 1 and 3 remain poorly matched by typical field dwarfs. For instance, source 1 is too blue at  $<1.2 \mu m$  and too red at  $>4 \mu m$  for a late-M field dwarf while source 3 has much weaker  $H_2O$  and  $CO$  at  $>2.5 \mu m$  than a field L dwarf (Figure 6), as discussed in Section 4.3. Therefore, we classify both objects as members of IC 348.

#### 4.5. Location of the Unidentified Hydrocarbon

What is the location of the carrier<sup>12</sup> producing the hydrocarbon features in the spectra of sources 1 and 3? The  $3.4 \mu m$  feature that arises from the diffuse ISM should be undetectable in sources 1 and 3 given their fairly low extinctions ( $A_V \lesssim 4$ , Figure 6) and the correlation between the optical depth of the feature and extinction in the diffuse ISM (Sandford et al. 1991; Pendleton et al. 1994; Chiar et al. 2000). Instead, these objects have much stronger  $3.4 \mu m$  absorption than sight lines with significantly higher extinctions ( $A_V \gtrsim 30$ ). In fact, sources 1 and 3 have the strongest  $3.4 \mu m$  features observed to date. Meanwhile, the absorption cross sections of hydrocarbons are typically  $\sim 10\text{--}100\times$  smaller for the overtone and combination bands than for the fundamental bands (e.g.,  $CH_4$ ; Hargreaves et al. 2020), which is one reason that they are not detected in the diffuse ISM (the other reason being the higher extinctions at the shorter wavelengths of those bands). In contrast, the overtone and combination bands in sources 1 and 3 are much stronger than implied by the absorption cross sections, which is indicative of the enhancement that occurs from radiative transfer in an optically thick atmosphere. Apart from the diffuse ISM, alternative absorbing media might include the molecular cloud that surrounds IC 348 or circumstellar material. However, the  $3.4 \mu m$  feature has not been detected in molecular clouds (Allamandola et al. 1992; Brooke et al. 1996; Chiar et al. 1996), protostellar envelopes (Boogert et al. 2015; McClure et al. 2023), or edge-on disks (Aikawa et al. 2012; Terada et al. 2012; Sturm et al. 2023). The absence of strong  $H_2O$  ice absorption at  $3 \mu m$  and the strength of the overtone and combination bands also argue against these locations for the hydrocarbon carrier. NIR spectra have been previously obtained for many members of IC 348 and field stars in the background of the cluster (Luhman et al. 1998, 2003, 2016), none of which show the overtone and combination bands that are detected in sources 1 and 3. Similarly, none of our NIRSpec targets that are clearly indicative of background objects show the  $3.4 \mu m$  feature. Thus, we conclude that the hydrocarbon detected in the spectra of sources 1 and 3 does not reside in foreground material, and instead is located in the atmospheres of the sources.

#### 4.6. The $3.4 \mu m$ Feature in Saturn and Titan

The detections of the  $3.4 \mu m$  absorption feature in sources 1 and 3 are the first in atmospheres outside of the solar system. Within the solar system, it has been detected in the atmospheres of Saturn and Titan through transmission spectroscopy performed by the Cassini mission. The  $3.4 \mu m$  feature and the overtone and combination bands in Saturn and Titan have been modeled in terms of  $CH_4$  and other hydrocarbons like  $C_2H_2$ ,  $C_2H_4$ , and  $C_2H_6$ , but a large component of the

<sup>12</sup> We refer to the carrier for the hydrocarbon features in the singular, but it may consist of multiple species among aliphatic hydrocarbons.

absorption must arise from an unidentified aliphatic hydrocarbon (Dalba et al. 2015; Maltagliati et al. 2015; Cours et al. 2020). In Figure 7, we show a transmission spectrum of Saturn (Dalba et al. 2015) for comparison to the hydrocarbon features in source 3. The profile of the  $3.4 \mu\text{m}$  feature in Titan is similar to that in Saturn (Bellucci et al. 2009). For reference, we have marked a wavelength of  $3.33 \mu\text{m}$  in Figure 7, which approximates the center of the strongest portion of the fundamental band of  $\text{CH}_4$ , the Q branch (see also Figure 2). As noted in the previous studies of the Cassini data, the blue wing of the  $3.4 \mu\text{m}$  feature in Saturn and Titan coincides with the  $\text{CH}_4$  Q branch, so some of the absorption can be attributed to  $\text{CH}_4$ . For sources 1 and 3, a local maximum occurs at the central wavelength of the Q branch, indicating little or no absorption from  $\text{CH}_4$ . Thus, unlike in Saturn and Titan, the overtone and combination bands in sources 1 and 3 should be entirely due to the unidentified hydrocarbon.

#### 4.7. Origin of the Hydrocarbons in Sources 1 and 3

We now discuss the origin of the hydrocarbons in sources 1 and 3. One possibility is that these objects inhabit a regime of physical properties that is previously unexplored (e.g., low temperature, low surface gravity, and thinning clouds), and the appearance of the unidentified hydrocarbons is typical for that regime (through an unknown process). In other words, the spectral differences between source 4 (a normal young L dwarf) and sources 1 and 3 may be analogous to the changes that occur from L types to T types among field dwarfs. The latter transition is characterized by the appearance of  $\text{CH}_4$ , a rapid shift to bluer NIR colors, and a strengthening of FeH at  $0.99 \mu\text{m}$  that follows a decline from L4 to L8 (Burgasser et al. 2002). Although photometric magnitudes are not perfectly correlated with spectral types among members of a star-forming region, the order of the three new members of IC 348 from brighter to fainter (4/1/3, Figure 4) may correspond to their order from higher to lower temperatures. Indeed, the spectrum of source 4 is similar to data for known young L dwarfs while other two objects show hydrocarbon features and are bluer at NIR wavelengths, which resembles the onset of methane and the shift to bluer colors for early T dwarfs in the field. FeH is weaker at lower surface gravities (McGovern et al. 2004) and is quite weak at all M/L types in star-forming regions (Luhman et al. 2017), so a strengthening across the L/T transition would not be expected for brown dwarfs in IC 348. However, source 1 does show a reemergence of TiO absorption at  $0.7\text{--}0.9 \mu\text{m}$ , which disappears at the M/L transition. Its  $\text{H}_2\text{O}$  bands are also indicative of M types (Figure 6). These spectral changes in source 1 relative to source 4 and other brighter brown dwarfs in IC 348 would represent a more radical reversal than found at the L/T transition among field dwarfs. Meanwhile, the faintest and potentially coolest of the three objects, source 3, suggests a rapid return to the red NIR colors of young L dwarfs and loss of the TiO bands. However, TWA 27B does not follow the pattern of these three objects given that it should be significantly cooler than source 1 (Section 5) and yet does not have the  $3.4 \mu\text{m}$  feature (Luhman et al. 2023). It is possible that this discrepancy is related to the difference in ages between IC 348 and TWA 27B (5 and 10 Myr, respectively) or indicates that the spectra are affected by a process that is not perfectly correlated with temperature (e.g., cloud thinning). Obviously, a larger sample of objects is needed to reliably characterize the pattern of spectral changes across the L/T transition at these young ages.

Several explanations have been proposed for the spectral changes across the L/T transition among field dwarfs (Ackerman & Marley 2001; Burgasser et al. 2002; Marley et al. 2002, 2010; Burrows et al. 2006; Tsuji & Nakajima 2003; Knapp et al. 2004; Tremblin et al. 2016; Charnay et al. 2018), most of which involve a decrease in cloud opacity. Models of that kind are able to reproduce some of the trends observed across the L/T transition, although they are not yet fully consistent with observations (Buenzli et al. 2015; Tremblin et al. 2016). In the case of the new brown dwarfs in IC 348, no existing models have predicted the hydrocarbon features in sources 1 and 3 or the brief reemergence of TiO and the weakening of  $\text{H}_2\text{O}$  bands in source 1.

As discussed above, sources 1 and 3 may represent typical examples of young brown dwarfs near the L/T transition. We can also speculate about alternative explanations for their hydrocarbon features. For instance, hydrocarbons can be produced in photochemistry that is driven by external UV radiation (Yoon et al. 2014; Moses et al. 2016; Zahnle et al. 2016; Carrasco et al. 2018; He et al. 2019; Helling et al. 2020). Since other members of IC 348 at earlier spectral types do not show the overtone and combination bands in their NIR spectra, that photochemical process (whatever it may be) must occur only in a low temperature range that encompasses sources 1 and 3. Possible sources of the UV radiation include the most massive member of IC 348, HD 281159 (B5V; Harris et al. 1954), and accretion shocks on the surfaces of the two objects if they have circumstellar disks. Sources 1 and 3 have projected separations of 0.22 and 0.13 pc from HD 281159, respectively. Based on a spectrum from the International Ultraviolet Explorer, the flux of HD 281159 between  $1200\text{--}2000 \text{ \AA}$  at a distance of 0.2 pc is a factor of  $\sim 1300$  lower than that received by Saturn during solar minimum (Woods & Rottman 2002). As mentioned in Section 4.2, the  $3.4 \mu\text{m}$  feature has been detected in meteorites and solar system dust, suggesting that the carrier may be present in circumstellar disks. Indeed, spectra at  $5\text{--}10 \mu\text{m}$  have detected emission features from  $\text{C}_2\text{H}_2$  and other hydrocarbons in disks around low-mass stars and brown dwarfs (Dahm & Carpenter 2009; Pascucci et al. 2009, 2013; Tabone et al. 2023). Therefore, a second scenario could involve the hydrocarbons originating in disks around the brown dwarfs and surviving accretion onto the photospheres. Recent studies have considered analogous situations in which young planetary companions accrete dust from the debris disks around their parent stars (Arras et al. 2022) and their spectra are affected by the accreted dust (Madurowicz et al. 2023). One final possibility is that sources 1 and 3 are ejected planets and their hydrocarbon features are related to their formation process in circumstellar disks. We consider this scenario to be unlikely given the low occurrence rate of massive gas giants (Howard et al. 2010), particularly for low-mass stars (Pass et al. 2023), and the short amount of time that has been available for the formation and ejection of planets in IC 348 ( $\sim 5$  Myr; Section 5). It is unclear how any of these alternative scenarios would account for the M-type features in source 1.

The identity of the hydrocarbon that produces the  $3.4 \mu\text{m}$  feature and the NIR overtone and combination bands in sources 1 and 3 can be better constrained through spectroscopy of those features at higher resolution and spectroscopy of additional hydrocarbon features beyond  $5 \mu\text{m}$  (Pendleton & Allamandola 2002). In addition, JWST spectra of additional objects with young ages and low temperatures, both

free-floating brown dwarfs and planetary companions, would help to determine whether the hydrocarbon features are a natural result of the L/T transition at very young ages or whether they arise from more exotic scenarios.

If young brown dwarfs do shift to bluer optical and NIR colors for some range of physical properties as implied by source 1, then such objects would be susceptible to rejection in brown dwarf surveys that use color–magnitude diagrams in that wavelength range. For instance, as mentioned in Section 2.3, source 1 was detected in deep optical imaging with WFPC2. In the resulting color–magnitude diagram (Luhman et al. 2005), its relatively blue color placed it below the sequence of known members, which suggested that it was a field star rather than a substellar member of the cluster.

The onset of the prominent hydrocarbon features in the spectra of sources 1 and 3 could be used to define a spectral type, and T is an option for the designation of that class, even if the hydrocarbon is not the one that defines T dwarfs at older ages ( $\text{CH}_4$ ). Nevertheless, we refrain from assigning spectral classes to sources 1 and 3 until more objects with the same hydrocarbon features are identified.

### 5. Physical Properties of New Brown Dwarfs

To characterize the physical properties of the three new members of IC 348 (sources 1, 3, and 4), we began by estimating their luminosities from a combination of the NIRSpect data (0.6–5.3  $\mu\text{m}$ ) and model spectra at other wavelengths. The NIRSpect data need to be corrected for extinction when deriving the luminosities. Extinctions for young stars are typically estimated by comparing their observed colors or spectra to the typical intrinsic measurements for young stellar photospheres at the spectral type in question. However, that approach is not reliably applicable to the new members of IC 348. Source 4 resembles previously observed young L dwarfs, but because of a degeneracy between spectral type and reddening in the NIR classification of young L dwarfs (Luhman et al. 2017), its intrinsic slope is uncertain. Meanwhile, sources 1 and 3 may inhabit previously unexplored ranges of spectral types and ages (Section 4.7), so we have no means of estimating their intrinsic slopes. Therefore, we assume that the extinction of each object is between  $A_V=0\text{--}4$ , which spans the values for most known members of the cluster (Luhman et al. 2016). To correct the NIRSpect data for extinction, we applied the extinction law from Schlafly et al. (2016). We calculated the luminosity of each object by integrating the extinction-corrected NIRSpect data and a model spectrum at shorter and longer wavelengths. We used the ATMO models of cloudless brown dwarfs (Tremblin et al. 2015, 2017; Petrus et al. 2023) and we adopted a distance of 313 pc, which is the weighted mean of distances from Gaia DR3 (Bailer-Jones et al. 2021) for the 40 known members that have the most accurate parallaxes ( $\sigma_\pi \lesssim 0.06$  mas). The standard error in that mean distance is  $\sim 0.6$  pc while the radius of the cluster is  $\sim 1$  pc based on its angular size. The corresponding uncertainties in the distances of sources 1, 3, and 4 (when assumed to be cluster members) contribute negligibly to the luminosity errors relative to the uncertainties in extinctions. The luminosity estimates are included in Table 1.

We can convert the luminosity estimates to effective temperatures and masses using the luminosities predicted by evolutionary models for an adopted age. The  $M_K$  offset between the sequences of low-mass stars in IC 348 and Upper

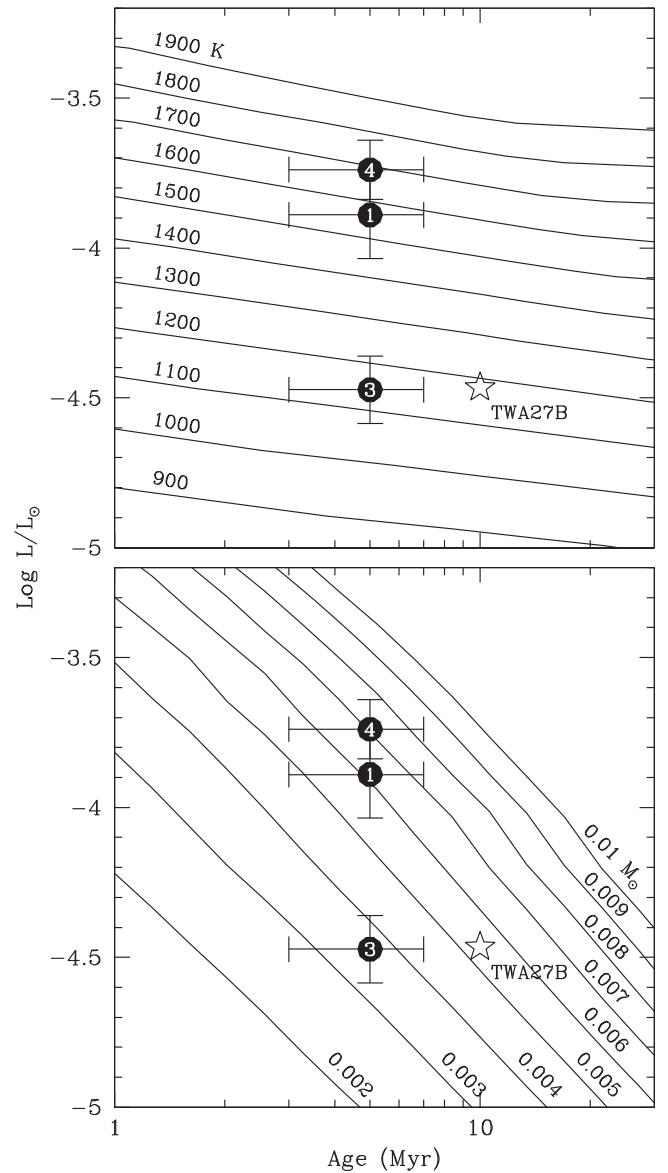


**Figure 8.** Luminosity estimates for new members of IC 348 identified with JWST (this work) compared to luminosities as a function of age predicted by the evolutionary models of Chabrier et al. (2023) for constant values of temperature and mass. For reference, we have included a luminosity estimate for the planetary mass companion TWA 27B (open star; Luhman et al. 2023).

Sco (Luhman et al. 2016) implies that IC 348 has an age of  $\sim 5$  Myr if we adopt a distance of 313 pc for IC 348, an age of 11 Myr for Upper Sco (Luhman & Esplin 2020), and  $\Delta \log L / \Delta \log \text{age} = -0.6$  (Baraffe et al. 2015; Choi et al. 2016; Dotter 2016; Feiden 2016). We have adopted an age uncertainty of 2 Myr. We have plotted the three new members of IC 348 in diagrams of luminosity versus age in Figure 8 with the luminosities predicted by the models of Chabrier et al. (2023) for constant values of temperature and mass. Similar luminosities are predicted by the models of Burrows et al. (1997) and Marley et al. (2021). The derived temperatures and masses for the three objects range from 1100 to 1800 K and 0.003–0.008  $M_{\odot}$  (3–8  $M_{\text{Jup}}$ ), respectively. For reference, we have included in Figure 8 a recent luminosity estimate for TWA 27B that is based on NIRSpect data (Luhman et al. 2023). The luminosity estimates and models imply that source 3 has a lower mass than TWA 27B and a roughly similar temperature.

Since evolutionary models of brown dwarfs are untested at young ages and planetary masses, the mass estimates for the new members of IC 348 are subject to systematic errors. The mass of source 1 is particularly uncertain given its anomalous M-type spectral features, which would normally be indicative of a low-mass star. We note that the magnitude limits of our spectroscopic sample (Figure 4) correspond to  $\sim 2 M_{\text{Jup}}$  for members of the cluster according to the adopted evolutionary models.

Mass estimates for young brown dwarfs have systematic errors that can differ from one study to another (e.g., different adopted models) and rely on the evidence of membership in a given cluster or association (via the adopted age), which can make it difficult to reliably compare the masses reported for planetary mass brown dwarfs. Nevertheless, source 3 appears to be a strong contender for the least massive free-floating brown dwarf that has been directly imaged to date. As mentioned in Section 1, microlensing surveys have indirectly detected a population of free-floating objects at much lower masses than source 3 (Gould et al. 2022).

In our previous surveys for brown dwarfs in IC 348, we have typically adopted an age of 3 Myr and the luminosities predicted by Chabrier et al. (2000) when estimating masses (e.g., Alves de Oliveira et al. 2013; Luhman et al. 2016). In this work, we have adopted an older age and models that predict lower luminosities for some ages and masses of young brown dwarfs, both of which lead to higher mass estimates relative to those that would be derived in our earlier studies.

## 6. Conclusions

We have used imaging and spectroscopy with JWST to search for planetary mass brown dwarfs in the center of the nearby star-forming cluster IC 348 ( $\sim 5$  Myr,  $\sim 300$  pc). Our results are summarized as follows:


1. We have obtained NIRCcam images of a  $6'0 \times 4'2$  field in the center of IC 348 in six filters between 1 and  $5 \mu\text{m}$ . This field encompasses 95 ( $\sim 20\%$ ) of the known members of the cluster. We have used the images to identify candidates for substellar members based on point-like flux profiles and positions in color–magnitude and color–color diagrams. The faintest candidates would have masses of  $\sim 2 M_{\text{Jup}}$  if they were members of IC 348 according to evolutionary models (Chabrier et al. 2023).
2. Using the MOS mode of NIRSpec, we have performed low-resolution spectroscopy ( $0.6\text{--}5.3 \mu\text{m}$ ) on four promising candidates, four lower-quality candidates, and one known late-type member. Three of the promising candidates (sources 1, 3, and 4) exhibit strong molecular absorption bands that indicate late spectral types while the remaining five candidates are likely to be background objects. The brightest of the three late-type candidates, source 4, is similar to known young L dwarfs in its spectral features, so we classify it as a member of IC 348. The other two candidates, sources 1 and 3, share several features that do not appear in source 4, most notably a strong absorption band near  $3.4\text{--}3.5 \mu\text{m}$  that coincides with the so-called  $3.4 \mu\text{m}$  feature that has been previously observed in the diffuse ISM and in the atmospheres of Saturn and Titan. That feature has been attributed to fundamental stretching modes of C–H in an unidentified aliphatic hydrocarbon.
3. To isolate the features in sources 1 and 3 that are anomalous, we have divided their spectra by data for normal young objects. The resulting spectra contain four prominent features between  $1.1\text{--}2.6 \mu\text{m}$  that align with the overtone and combination bands of C–H stretching modes in hydrocarbons. We conclude that these bands arise from the same carrier that produces the fundamental band at  $3.4 \mu\text{m}$ . Thus, most of the features in the spectra of sources 1 and 3 that are anomalous relative to known young late-type objects are explained by an unidentified hydrocarbon, whether it resides in their atmospheres or the ISM. Meanwhile, even after accounting for the hydrocarbon features, source 1 and 3 remain poorly matched by typical field dwarfs. Therefore, we classify both objects as members of IC 348.
4. We have considered whether the hydrocarbons observed toward sources 1 and 3 arise from their atmospheres or foreground material in the diffuse ISM, the molecular cloud surrounding IC 348, a protostellar envelope, or an edge-on disk. We conclude that the hydrocarbons very likely reside in the atmospheres of these objects for the following reasons: (1) the extinctions of sources 1 and 3 are far too low for their  $3.4 \mu\text{m}$  features to arise from the diffuse ISM. Given their extinctions, absorption from the diffuse ISM should be undetectable, and yet their  $3.4 \mu\text{m}$  features are stronger than any previously observed in the diffuse ISM; (2) previous studies have not detected the  $3.4 \mu\text{m}$  feature in molecular clouds, protostellar envelopes, or edge-on disks, and sources 1 and 3 lack the deep  $3 \mu\text{m}$  H<sub>2</sub>O ice band that typically appears in the latter two scenarios; and (3) the strengths of the overtone and combination bands indicate an origin in atmospheres rather than a foreground medium. Thus, the detections of the  $3.4 \mu\text{m}$  feature in sources 1 and 3 are the first in atmospheres outside of the solar system.
5. We have discussed possible origins for the hydrocarbons in sources 1 and 3, which are not predicted by any models of young brown dwarfs. In the scenario that we tend to favor, these objects have a combination of physical properties (e.g., low temperature, low surface gravity, and thinning clouds) that has not been observed previously and that, through an unknown mechanism, enables the formation of the unidentified hydrocarbon (and little or no methane). In this way, sources 1 and 3 may reside near a transition at young ages that is analogous to the L/T transition among older dwarfs in the field. M-type features in source 1 (TiO and moderate H<sub>2</sub>O), which is much too faint for a normal M-type cluster member, might also be a natural consequence of that transition. However, we have no physical explanation for how the L/T transition at young ages would give rise to a nonmethane hydrocarbon and the M-type features of source 1. In addition, the spectrum of the young planetary mass companion TWA 27B does not follow the pattern of changes with temperature that is implied by the three new members of IC 348. JWST spectra of a larger sample of young substellar objects (both brown dwarfs and planets) are needed to better constrain the origin of the hydrocarbon features in sources 1 and 3.
6. Luminosities have been estimated for the three new members of IC 348 from the NIRSpec data and model spectra at other wavelengths. We have converted those

luminosities to temperatures and masses using evolutionary models (Chabrier et al. 2023), arriving at values that range from 1100 to 1800 K and 3–8  $M_{\text{Jup}}$ , respectively. The mass estimate for source 1 is uncertain given its anomalous M-type spectral features. The faintest object, source 3, is a strong contender for the least massive free-floating brown dwarf that has been directly imaged to date.

### Acknowledgments

We thank Adwin Boogert, Nuria Calvet, Michael Cushing, Emmanuel Dartois, Peter Gao, Robert Hargreaves, Christiane Helling, Matthew Izawa, Katharina Lodders, Mark Marley, Julianne Moses, Xander Tielens, and Ewine van Dishoeck for helpful discussions. P.T. acknowledges support from the European Research Council under grant agreement ATMO 757858. R.P. acknowledges support from the Royal Society in the form of a Dorothy Hodgkin Fellowship. The JWST data were obtained from MAST at the Space Telescope Science Institute, which is operated by the Association of Universities for Research in Astronomy, Inc., under NASA contract NAS 5-03127. The JWST observations are associated with program 1229. This work made use of ESA Datalabs (<https://datalabs.esa.int>), which is an initiative by ESA's Data Science and Archives Division in the Science and Operations Department, Directorate of Science. This work used data from the ESA mission Gaia (<https://www.cosmos.esa.int/gaia>), processed by the Gaia Data Processing and Analysis Consortium (DPAC; <https://www.cosmos.esa.int/web/gaia/dpac/consortium>). Funding for the DPAC has been provided by national institutions, in particular the institutions participating in the Gaia Multilateral Agreement. The Center for Exoplanets and Habitable Worlds is supported by the Pennsylvania State University, the Eberly College of Science, and the Pennsylvania Space Grant Consortium.

### ORCID iDs

K. L. Luhman  <https://orcid.org/0000-0003-2822-2951>  
 C. Alves de Oliveira  <https://orcid.org/0000-0003-2896-4138>  
 I. Baraffe  <https://orcid.org/0000-0001-8365-5982>  
 G. Chabrier  <https://orcid.org/0000-0002-8342-9149>  
 T. R. Geballe  <https://orcid.org/0000-0003-2824-3875>  
 R. J. Parker  <https://orcid.org/0000-0002-1474-7848>  
 Y. J. Pendleton  <https://orcid.org/0000-0001-8102-2903>  
 P. Tremblin  <https://orcid.org/0000-0001-6172-3403>

### References

- Ackerman, A. S., & Marley, M. S. 2001, *ApJ*, 556, 872  
 Aikawa, Y., Kamuro, D., Sakon, I., et al. 2012, *A&A*, 538, A57  
 Allamandola, L. J., Sandford, S. A., Tielens, A. G. G. M., & Herbst, T. M. 1992, *ApJ*, 399, 134  
 Allers, K. N., & Liu, M. C. 2020, *PASP*, 132, 104401  
 Alves de Oliveira, C., Birkmann, S. M., Böker, T., et al. 2018, *Proc. SPIE*, 10704, 107040Q  
 Alves de Oliveira, C., Moraux, E., Bouvier, J., et al. 2013, *A&A*, 549, A123  
 Alves de Oliveira, C., Moraux, E., Bouvier, J., & Bouy, H. 2012, *A&A*, 539, A151  
 Arras, P., Wilson, M., Pryal, M., & Baker, J. 2022, *ApJ*, 932, 90  
 Bailer-Jones, C. A. L., Rybizki, J., Fousneau, M., Demleitner, M., & Andrae, R. 2021, *AJ*, 161, 147  
 Baraffe, I., Horneier, D., Allard, F., & Chabrier, G. 2015, *A&A*, 577, 42  
 Bardalez Gagliuffi, D. C., Faherty, J. K., Schneider, A. C., et al. 2020, *ApJ*, 895, 145  
 Bellucci, A., Sicardy, B., Drossart, P., et al. 2009, *Icar*, 201, 198  
 Böker, T., Beck, T. L., Birkmann, S. M., et al. 2023, *PASP*, 135, 038001  
 Boogert, A. C., Gerakines, P. A., & Whittet, D. C. B. 2015, *ARA&A*, 53, 541  
 Bouy, H., Tamura, M., Barrado, D., et al. 2022, *A&A*, 664, A111  
 Brooke, T. Y., Sellgren, K., & Smith, R. G. 1996, *ApJ*, 459, 209  
 Buenzli, E., Saumon, D., Marley, M. S., et al. 2015, *ApJ*, 798, 127  
 Burgasser, A. J. 2007, *ApJ*, 659, 655  
 Burgasser, A. J., Marley, M. S., Ackerman, A. S., et al. 2002, *ApJL*, 571, L151  
 Burrows, A., Marley, M., Hubbard, W. B., et al. 1997, *ApJ*, 491, 856  
 Burrows, A., Sudarsky, D., & Hubeny, I. 2006, *ApJ*, 640, 1063  
 Butchart, I., McFadzean, A. D., Whittet, D. C. B., Geballe, T. R., & Greenberg, J. M. 1986, *A&A*, 154, L5  
 Carrasco, N., Tigrine, S., Gavilan, L., Nahon, L., & Gudipati, M. S. 2018, *NatAs*, 2, 489  
 Chabrier, G., Baraffe, I., Allard, F., & Hauschildt, P. 2000, *ApJ*, 542, 464  
 Chabrier, G., Baraffe, I., Phillips, M., & Debras, F. 2023, *A&A*, 671, A119  
 Chabrier, G., & Lenoble, R. 2023, *ApJL*, 944, L33  
 Charnay, B., Bézard, B., Baudino, J.-L., et al. 2018, *ApJ*, 854, 172  
 Chauvin, G., Lagrange, A.-M., Dumas, C., et al. 2004, *A&A*, 425, L29  
 Chiar, J. E., Adamson, A. J., & Whittet, D. C. B. 1996, *ApJ*, 472, 665  
 Chiar, J. E., Pendleton, Y. J., Geballe, T. R., & Tielens, A. G. G. M. 1998, *ApJ*, 507, 281  
 Chiar, J. E., Tielens, A. G. G. M., Adamson, A. J., & Ricca, A. 2013, *ApJ*, 770, 78  
 Chiar, J. E., Tielens, A. G. G. M., Whittet, D. C. B., et al. 2000, *ApJ*, 537, 749  
 Choi, J., Dotter, A., Conroy, C., et al. 2016, *ApJ*, 823, 102  
 Clark, R. N., Curchin, J. M., Hoefen, T. M., & Swayze, G. A. 2009, *JGR*, 114, E03001  
 Cours, T., Cordier, D., Seignovert, B., Maltagliati, L., & Biennier, L. 2020, *Icar*, 339, 113571  
 Cruz, K. L., Kirkpatrick, J. D., & Burgasser, A. J. 2009, *AJ*, 137, 3345  
 Cruz, K. L., Núñez, A., Burgasser, A. J., et al. 2018, *AJ*, 155, 34  
 Cushing, M. C., Kirkpatrick, J. D., Gelino, C. R., et al. 2011, *ApJ*, 743, 50  
 Cushing, M. C., Rayner, J. T., & Vacca, W. D. 2005, *ApJ*, 623, 1115  
 Dahm, S. E., & Carpenter, J. M. 2009, *AJ*, 137, 4024  
 Dalba, P. A., Muirhead, P. S., Fortney, J. J., et al. 2015, *ApJ*, 814, 154  
 Dartois, E., Geballe, T. R., Pino, T., et al. 2007, *A&A*, 463, 635  
 de Bruijne, J. H. J. 2012, *Ap&SS*, 341, 31  
 de Vries, M. S., Reihls, K., Wendt, H. R., et al. 1993, *GeCoA*, 57, 933  
 Dotter, A. 2016, *ApJS*, 222, 8  
 Ehrenfreund, P., Robert, F., D'Hendecourt, L., & Behar, F. 1991, *A&A*, 252, 712  
 Esplin, T. L., & Luhman, K. L. 2017, *AJ*, 154, 134  
 Esplin, T. L., & Luhman, K. L. 2019, *AJ*, 158, 54  
 Esplin, T. L., Luhman, K. L., Faherty, J. K., Mamajek, E. E., & Bochanski, J. J. 2017, *AJ*, 154, 46  
 Feiden, G. A. 2016, *A&A*, 593, A99  
 Ferruit, P., Jakobsen, P., Giardino, G., et al. 2022, *A&A*, 661, A81  
 Filippazzo, J. C., Rice, E. L., Faherty, J., et al. 2015, *ApJ*, 810, 158  
 Gagné, J., Allers, K. N., Theissen, C. A., et al. 2018, *ApJ*, 854, L27  
 Gaia Collaboration, Brown, A. G. A., Vallenari, A., Prusti, T., et al. 2021, *A&A*, 649, A1  
 Gaia Collaboration, Prusti, T., de Bruijne, J. H. J., et al. 2016, *A&A*, 595, A1  
 Gaia Collaboration, Vallenari, A., Brown, A. G. A., et al. 2023, *A&A*, 674, A1  
 Gardner, J. P., Mather, J. C., Abbott, R., et al. 2023, *PASP*, 135, 068001  
 Gauza, B., Béjar, V. J. S., Pérez-Garrido, A., et al. 2015, *ApJ*, 804, 96  
 Geballe, T. R., Goto, M., Usuda, T., Oka, T., & McCall, B. J. 2006, *ApJ*, 644, 907  
 Geballe, T. R., Pendleton, Y., Chiar, J., & Tielens, A. G. G. M. 2021, *ApJ*, 912, 47  
 Gould, A., Jung, Y. K., Hwang, K.-H., et al. 2022, *JKAS*, 55, 173  
 Hargreaves, R. J., Gordon, I. E., Rey, M., et al. 2020, *ApJS*, 247, 55  
 Harris, D. L., Morgan, W. W., & Roman, N. G. 1954, *ApJ*, 119, 622  
 He, C., Hörst, S. M., Lewis, N. K., et al. 2019, *ESC*, 3, 39  
 Helling, Ch, Kawashima, Y., Graham, V., et al. 2020, *A&A*, 641, A178  
 Herbig, G. H. 1998, *ApJ*, 497, 736  
 Herbst, W. 2008, in *Handbook of Star Forming Regions*, Vol. 1, The Northern Sky, ASP Monograph Series 4, ed. B. Reipurth (San Francisco, CA: ASP), 372  
 Hinkley, S., Carter, A. L., Ray, S., et al. 2022, *PASP*, 134, 095003  
 Howard, A., Marcy, G. W., Johnson, J. A., et al. 2010, *Sci*, 330, 653  
 Izawa, M. R. M., Applin, D. M., Norman, L., & Cloutis, E. A. 2014, *Icar*, 237, 159  
 Jakobsen, P., Ferruit, P., Alves de Oliveira, C., et al. 2022, *A&A*, 661, A80

- Keller, L. P., Bajt, S., Baratta, G. A., et al. 2006, *Sci*, 314, 1728
- Kellogg, K., Metchev, S., Geißler, K., et al. 2015, *AJ*, 150, 182
- Kim, H.-W., Hwang, K.-H., Gould, A., et al. 2021, *AJ*, 162, 15
- Kim, S. J., Sim, C. K., Lee, D. W., et al. 2012, *P&SS*, 65, 122
- Kirkpatrick, J. D., Cushing, M. C., Gelino, C. R., et al. 2011, *ApJS*, 197, 19
- Kirkpatrick, J. D., Martin, E. C., Smart, R. L., et al. 2019, *ApJS*, 240, 19
- Knapp, G. R., Leggett, S. K., Fan, X., et al. 2004, *AJ*, 127, 3553
- Lacy, J. H., Baas, F., Allamandola, L. J., et al. 1984, *ApJ*, 276, 533
- Lada, E. A., & Lada, C. J. 1995, *AJ*, 109, 1682
- Lalchand, B., Chen, W.-P., Biller, B. A., et al. 2022, *AJ*, 164, 125
- Lequeux, J., & Jourdain de Muizon, M. 1990, *A&A*, 240, L19
- Li, J., Long, L., Zhong, J., et al. 2023, *ApJS*, 266, 4
- Liu, M. C., Dupuy, T. J., & Allers, K. N. 2016, *ApJ*, 833, 96
- Liu, M. C., Magnier, E. A., Deacon, N. R., et al. 2013, *ApJ*, 777, L20
- Lodieu, N., Zapatero Osorio, M. R., Béjar, V. J. S., & Peña Ramírez, K. 2018, *MNRAS*, 473, 2020
- Lucas, P. W., Roche, P. F., Allard, F., & Hauschildt, P. H. 2001, *MNRAS*, 326, 695
- Luhman, K. L. 2014, *ApJ*, 786, L18
- Luhman, K. L. 2023, *AJ*, 165, 269
- Luhman, K. L., Esplin, T. E., & Loutrel, N. P. 2016, *ApJ*, 827, 52
- Luhman, K. L., & Esplin, T. L. 2020, *AJ*, 160, 44
- Luhman, K. L., & Hapich, C. J. 2020, *AJ*, 160, 57
- Luhman, K. L., Mamajek, E. E., Shukla, S. J., & Loutrel, N. P. 2017, *AJ*, 153, 46
- Luhman, K. L., McLeod, K. K., & Goldenson, N. 2005, *ApJ*, 623, 1141
- Luhman, K. L., Rieke, G. H., Lada, C. J., & Lada, E. A. 1998, *ApJ*, 508, 347
- Luhman, K. L., Stauffer, J. R., Muench, A. A., et al. 2003, *ApJ*, 593, 1093
- Luhman, K. L., Tremblin, P., Birkmann, S. M., et al. 2023, *ApJL*, 949, L36
- Madurowicz, A., Mukherjee, S., Batalha, N., Macintosh, B., Marley, M., & Karalidi, T. 2023, *AJ*, 165, 238
- Maltagliati, L., Bézard, B., Vinatier, S., et al. 2015, *Icar*, 248, 1
- Marley, M. S., Saumon, D., & Goldblatt, C. 2010, *ApJL*, 723, L117
- Marley, M. S., Saumon, D., Visscher, C., et al. 2021, *ApJ*, 920, 85
- Marley, M. S., Seager, S., Saumon, D., et al. 2002, *ApJ*, 568, 335
- Matrajt, G., Muñoz Caro, G. M., Dartois, E., et al. 2005, *A&A*, 433, 979
- McClure, M. K., Rocha, W. R. M., Pontoppidan, K. M., et al. 2023, *NatAs*, 7, 431
- McGovern, M. R., Kirkpatrick, J. D., McLean, I. S., et al. 2004, *ApJ*, 600, 1020
- Meisner, A. M., Caselden, D., Kirkpatrick, J. D., et al. 2020, *ApJ*, 889, 74
- Miles, B. E., Biller, B. A., Patapis, P., et al. 2023, *ApJL*, 946, L6
- Moses, J. I., Marley, M. S., Zahnle, K., et al. 2016, *ApJ*, 829, 66
- Mróz, P., Udalski, A., Skowron, J., et al. 2017, *Natur*, 548, 183
- Pascucci, I., Apai, D., Luhman, K., et al. 2009, *ApJ*, 696, 143
- Pascucci, I., Herczeg, G., Carr, J. S., & Bruderer, S. 2013, *ApJ*, 779, 178
- Pass, E. K., Winters, J. G., Charbonneau, D., et al. 2023, *AJ*, 166, 11
- Pendleton, Y. J., & Allamandola, L. J. 2002, *ApJS*, 138, 75
- Pendleton, Y. J., Sandford, S. A., Allamandola, L. J., Tielens, A. G. G. M., & Sellgren, K. 1994, *ApJ*, 437, 683
- Pendleton, Y. J., Tielens, A. G. G. M., Tokunaga, A. T., & Bernstein, M. P. 1999, *ApJ*, 513, 294
- Perryman, M. A. C., de Boer, K. S., Gilmore, G., et al. 2001, *A&A*, 369, 339
- Petrus, S., Chauvin, G., Bonnefoy, M., et al. 2023, *A&A*, 670, L9
- Rayner, J. T., Cushing, M. C., & Vacca, W. D. 2009, *ApJS*, 185, 289
- Rieke, M. J., Kelly, D. M., & Horner, S. 2005, *Proc. SPIE*, 5904, 590401
- Rieke, M. J., Kelly, D. M., Misselt, K., et al. 2023, *PASP*, 135, 028001
- Robberto, M., Gennaro, M., Giulia Ubeira Gabellini, M., et al. 2020, *ApJ*, 896, 79
- Robinson, T. D., Maltagliati, L., Marley, M. S., & Fortney, J. J. 2014, *PNAS*, 111, 9042
- Ryu, Y.-H., Mróz, P., Gould, A., et al. 2021, *AJ*, 161, 126
- Sandford, S. A., Aléon, J., Alexander, C. M. O. D., et al. 2006, *Sci*, 314, 1720
- Sandford, S. A., Allamandola, L. J., Tielens, A. G. G. M., et al. 1991, *ApJ*, 371, 607
- Schlafly, E. F., Meisner, A. M., Stutz, A. M., et al. 2016, *ApJ*, 821, 78
- Schneider, A. C., Burgasser, A. J., Bruursema, J., et al. 2023, *ApJ*, 943, L16
- Schneider, A. C., Windsor, J., Cushing, M. C., Kirkpatrick, J. D., & Wright, E. L. 2016, *ApJ*, 822, L1
- Scholz, A., Jayawardhana, R., Muzic, K., et al. 2012, *ApJ*, 756, 24
- Soifer, B. T., Russell, R. W., & Merrill, K. M. 1976, *ApJL*, 207, L83
- Sorahana, S., & Yamamura, I. 2012, *ApJ*, 760, 151
- Sturm, J. A., McClure, M. K., Beck, T. L., et al. 2023, *A&A*, in press
- Tabone, B., Bettoni, G., van Dishoeck, E. F., et al. 2023, *NatAs*, 7, 805
- Terada, H., Tokunaga, A. T., Pyo, T.-S., et al. 2012, *AJ*, 144, 175
- Tremblin, P., Amundsen, D. S., Chabrier, G., et al. 2016, *ApJL*, 817, L19
- Tremblin, P., Amundsen, D. S., Mourier, P., et al. 2015, *ApJL*, 804, L17
- Tremblin, P., Chabrier, G., Baraffe, I., et al. 2017, *ApJ*, 850, 46
- Tsuji, T., & Nakajima, T. 2003, *ApJL*, 585, L151
- Wdowiak, T. J., Flickinger, G. C., & Cronin, J. R. 1988, *ApJL*, 328, L75
- Willner, S. P., Russell, R. W., Puetter, R. C., Soifer, B. T., & Harvey, P. M. 1979, *ApJL*, 229, L65
- Woods, T. N., & Rottman, G. J. 2002, in *Atmospheres in the Solar System: Comparative Aeronomy*, Geophysical Monograph 130, ed. M. Mendillo, A. Nagy, & J. H. Waite (Washington, DC: American Geophysical Union), 221
- Wright, G. S., Bridger, A., Geballe, T. R., & Pendleton, Y. 1996, in *New Extragalactic Perspectives in the New South Africa*, ed. D. L. Block & J. M. Greenberg (Dordrecht: Kluwer), 143
- Yoon, Y. H., Hörst, S. M., Hicks, R. K., et al. 2014, *Icar*, 233, 233
- Zahnle, K., Marley, M. S., Morley, C. V., & Moses, J. I. 2016, *ApJ*, 824, 137
- Zapatero Osorio, M. R., Béjar, V. J. S., & Peña Ramírez, K. 2017, *ApJ*, 842, 65